HHS Public Access

Author manuscript

ACS Nano. Author manuscript; available in PMC 2022 November 11.

Published in final edited form as:

ACS Nano. 2021 August 24; 15(8): 13289–13306. doi:10.1021/acsnano.1c03035.

Long-term, Non-invasive *in Vivo* Tracking of Progenitor Cells Using Multimodality Photoacoustic, Optical Coherence Tomography, and Fluorescence Imaging

Phuc Van Nguyen[1,§], **Wen Fan**[1,4,§], **Tianye Zhu**[1,4], **Wei Qian**[2], **Yanxiu Li**[1], **Bing Liu**[2], **Wei Zhang**[3], **Jessica Henry**[1], **Songtao Yuan**[4], **Xueding Wang**[3,*], **Yannis M. Paulus**[1,3,*]

[1]Department of Ophthalmology and Visual Sciences, University of Michigan, Ann Arbor, MI 48105, USA

[2]IMRA America Inc., Ann Arbor, MI 48105, USA

[3]Department of Biomedical Engineering, University of Michigan, Ann Arbor, MI 48105, USA

[4]Department of Ophthalmology, The First Affiliated Hospital of Nanjing Medical University, 210029, China

Abstract

Stem cell regenerative medicine therapies have emerged as promising treatments for currently incurable diseases. A remaining challenge for cell therapies is the ability to track the migration and distribution of the transplanted cells in a long-term, non-invasive manner *in vivo* to assess their efficacy. This study develops a non-invasive, and high spatial resolution photoacoustic microscopy (PAM) and optical coherence tomography (OCT) imaging system for *in vivo* tracking of subretinally injected progenitor human retinal pigment epithelium cells (ARPE-19) labeled with chain-like gold nanoparticle (CGNP) clusters in RPE damage. CGNP provided significant PAM, OCT, and fluorescence signal to selectively track the migration of ARPE-19 cells in living rabbit eyes for 3 months. PAM and OCT imaging allow accurate anatomical information to determine

[*]Corresponding Authors: Yannis M. Paulus, M.D., F.A.C.S., Department of Ophthalmology and Visual Sciences, Department of Biomedical Engineering, University of Michigan, 1000 Wall Street, Ann Arbor, MI 48105, USA, ypaulus@med.umich.edu, Xueding Wang, Ph.D., Department of Biomedical Engineering, Department of Radiology, University of Michigan, xdwang@umich.edu.
[§]These authors contributed equally to this work.

Author Contributions

V.P.N. designed the experiments, carried out tissue culture, maintenance and analysis, animal work, *in vitro* characterization, *in vivo* PAM, OCT, and ICG imaging, 3D image rendering, image segmentation and analysis of the *in vivo* images, and wrote the manuscript. T. Z and W.F. contributed to cell preparation and undertook the subretinal injection. W.Q. synthesized nanoparticle contrast agents, characterized their properties, performed cell imaging using dark field microscopy, and wrote the manuscript. B.L. established pulsed laser ablation setup for producing nanoparticles. Y.L. and J. H. assisted with histological analysis. W.Z. supported with maintenance the imaging system. X.W. and Y.M.P. supervised the project, organized and wrote the manuscript.

Supporting Information Available: The following files are available free of charge.

Supplementary Information Stem Cells Tracking using multimodal PAM and OCT imaging.docx Synthesis of CGNP cluster RGD protocol. Transmission electron microscopy (TEM). Particle's size distribution obtained from the TEM image. UV-Vis absorbance spectrum of CGNPs measured at different times. Fourier transformed infrared spectroscopy of PEG and CGNPs-RGD. PAM image of silicone tubes filled with CGNPs at various concentrations. B-scan OCT image of glass capillaries tubes poured with CGNPs at different concentrations. Confocal laser scanning microscopic images of cells treated with CGNPs-RGD without conjugation with RGD. Dark field imaging for cells treated with CGNPs. Real-time OCT guided subretinal delivery of labeled cells into the retina. *In vivo* multi-modality imaging of subretinal injection of unlabeled ARPE-19 cells. Image segmentation to quantify PAM signal amplitudes. *In vivo* photostability and spectroscopic PAM imaging. Fluorescence intensity. H&E and TUNEL images of organs

Competing interests

The authors declare no competing financial interests.

the exact retinal layer in which the transplanted ARPE-19 cells are located and is confirmed by histology. This presents a promising technology to visualize fundamental biological processes of cell therapies in complex *in vivo* environments in real time.

Keywords

stem cells; regenerative medicine; photoacoustic microscopy; optical coherence tomography; contrast agents; progenitor human retinal pigment epithelium cells; gold nanoparticles

Stem cell-based regenerative medicine therapies (RMTs) provide promising therapeutic approaches for serious injuries and currently incurable diseases that conventional medicines and therapies cannot effectively treat including stroke, cancer, Alzheimer's disease, cardiovascular disease, bone repair, Parkinson's disease, diabetes, and ocular diseases.[1–4] The major benefits of RMTs rely on their remarkable potential to replace or restore functionally damaged tissue through cell transplantation. To achieve these treatment capabilities, transplanted cells must home to the site of injury, survive, and differentiate into the target cells or multiple cell types. The retina of the eye, similar to central nervous system, involves neurons with limited to no regenerative capacity. Thus, if the retina is damaged, permanent blindness can result. Therefore, cell-based therapies have attracted significant attention for retinal diseases. Voretigene neparvovec-rzyl (Luxturna) was the first gene therapy approved by the US Food and Drug Administration (FDA) in December 2017 to treat biallelic RPE65 retinal degeneration.[5] Stem cell therapy has also attracted considerable interest and provides a great potential therapeutic method for treating degeneration of photoreceptors or retinal pigment epithelial (RPE) cell atrophy, which is a major cause of vision loss in patients with geographic atrophy from age-related macular degeneration (AMD). Currently, no effective therapeutic approach exists to treat this highly prevalent disorder. Hundreds of clinical trials of stem cell therapies for retinal diseases involving translocation of RPE cells *via* subretinal injection have been performed.[6–8] After subretinal injection, these cells can replicate themselves to replace the retinal pigment epithelium, which is necessary for the health of the photoreceptors. However, a major clinical challenge to evaluate treatment outcome is the lack of a comprehensive understanding of the fate, migration, viability, and function of the transplanted cells in the local microenvironment *in vivo.* Traditionally, histological analysis is often used to examine and evaluate cells after administration.[9,10] Due to its invasive nature, histological analysis only offers snapshots of the treatment process which, however, could be highly dynamic and both temporally and spatially heterogeneous. In addition, invasive histological analysis may not be an option for many clinical applications such as the treatment of aforementioned eye diseases. Therefore, it is a long-standing and serious need in RMTs to have advanced non-invasive imaging techniques which can longitudinally track the transplanted cells qualitatively and quantitatively *in vivo*.

Several imaging techniques have been developed for labeling and tracking the fate of transplanted cells such as fluorescence microscopy, bioluminescence, magnetic resonance imaging (MRI), positron emission tomography (PET), and single photon emission computed tomography (SPECT).[11–14] Although these methods provide non-invasive or minimally-

invasive techniques and easy accessibility, they also possess several limitations, including high-cost, limited resolution, and ionizing radiation associated with MRI, PET, and SPECT, respectively. To overcome these disadvantages, photoacoustic imaging has been explored as an emerging imaging modality for cell tracking due to its high sensitivity, excellent spatial resolution, and sufficient tissue penetration.[15–17] Furthermore, photoacoustic imaging can be easily combined with other optical imaging technologies, such as scanning laser ophthalmoscopy (SLO), fluorescence microscopy, and optical coherence tomography (OCT),[18–20] to present complementary diagnostic information. Except melanoma cells and red blood cells that have strong intrinsic optical absorption in the visible to near-infrared spectrum, most types of cells do not generate strong photoacoustic signals. Thus, to improve the sensitivity and to better monitor and track stem cells, exogenous contrast agents can be utilized. A number of nanoparticles and organic chromophores have been used as contrast agents for photoacoustic microscopy (PAM) and OCT imaging.[15–17,21] Dhada and Donnelly *et al.* labeled mesenchymal stem cells (MSCs) with gold nanoparticles (GNPs) for tracking them *in vivo* using photoacoustic imaging,[15,16] and found that GNPs had no adverse effects on cell functions, including proliferation, viability, and differentiation *in vitro*. Recently, in a study performed *ex vivo* in pig eyes, GNPs were also used to label MSCs for photoacoustic image-guided delivery in the retina.[22] Because the optical absorption peak of the GNPs used in that work overlapped with that of hemoglobin, distinguishing stem cells from native blood vessels turned out to be difficult.

In this study, a non-invasive, non-ionizing, high spatial resolution PAM and OCT multimodality imaging system was developed and utilized to monitor cells delivered into the subretinal space and track these cells longitudinally post-injection. The transplanted human retinal pigment epithelium cells (ARPE-19) were labelled with chain-like gold nanoparticle (CGNP) clusters which were non-toxic and biocompatible and showed excellent photostability and colloidal stability both *in vivo* and *in vitro*. Theses CGNP clusters were fabricated through assembling spherical GNPs physically produced using a method of femtosecond pulsed laser ablation of bulk gold target in deionized water to avoid toxicities associated with precursors, stabilizers, and surfactants used in chemical synthesis. *In vivo* PAM and OCT imaging using a rabbit model of laser-induced RPE damage in the retina was implemented to investigate the feasibility of this imaging technology for guiding RMTs. Longitudinal PAM tracking of transplanted ARPE-19 cells was conducted for up to 3 months post-injection, and signal amplitudes were quantitatively measured to determine the migration of the ARPE-19 cells *in vivo*. At the same time, OCT imaging was performed to guide the subretinal injection and to monitor the regeneration of the damaged RPE layer as well as the migration of the ARPE-19 cells.

Results and Discussion

PAM, OCT, and fluorescence multimodality molecular imaging system:

The custom-built multimodality imaging platform shown in Fig. 1A offers several benefits regarding high spatial resolution, fast image acquisition, real-time image-guidance, and non-invasiveness. As demonstrated previously, the lateral resolutions of PAM and OCT are 4.1 and 3.8 μm and the axial resolutions are estimated to be 37.0 μm for PAM and 4.0

μm for OCT, respectively.[23] Fast image acquisition is important to achieve high resolution PAM imaging with minimal motion artifacts. It takes approximately 65 s to obtain a volumetric image of 5×5 mm^2 with a resolution of 256×256 pixels. The imaging system is suitable to detect the biodistribution and migration of ARPE-19 cells labeled with CGNP clusters after delivery into the subretinal space of rabbits having localized RPE damage *via* photocoagulation lesions.

Contrast agent characterization and *in vitro* cell labeling.

Multifunctional CGNP clusters used to label progenitor ARPE-19 cells for multi-modality PAM, OCT, and fluorescence microscopy imaging were successfully synthesized as shown in Fig. 1B. Colloidal suspension of GNPs was produced by physical method of femtosecond pulsed laser ablation of gold target in DI water (see Supplementary Information). The average diameter of GNPs was estimated to be 20±4 nm and verified by TEM (Fig. S1A–B). These GNP monomers were self-assembled into CGNP clusters after modifying their surface with both pentapeptide Cys-Ala-Leu-Asn-Asn (CALNN) and cysteamine ligands (see Supplementary Information for more details). Then, the surface of CGNP clusters were conjugated with RGD peptides (CGNP clusters-RGD) and further modified with near-infrared indocyanine green (ICG) fluorescent chromophore (ICG-CGNP clusters-RGD). The morphology of the synthesized CGNP clusters-RGD was assessed by transmission electron microscopy (TEM) as shown in Figure 2A. The synthesized CGNP clusters had a red-shifted absorption peak at 650 nm compared to that at 520 nm for the GNP monomers (Fig. 2B). CGNP clusters-RGD showed excellent photostability after being illuminated by 65,536 shots of 650 nm nanosecond pulsed laser at different fluences of 0.005, 0.01, 0.02, and 0.04 mJ/cm^2, respectively (Fig. 2C). The average size, hydrodynamic diameter, and zeta potential of CGNP clusters were determined using TEM and zeta sizer. The CGNP clusters had an average size of 64±21 nm in length and 20±4 nm in width (Fig. 2D and Fig. S1C). The zeta potentials of CGNP clusters-RGD and ICG-CGNP clusters-RGD were −41±3 mV and −39±3 mV, respectively. The large negative zeta potential leads to excellent colloidal stability with a shelf life of longer than three months (Fig. S1D). Hydrodynamic diameter results were used to further verify conjugation of RGD and ICG on the surface of the CGNP clusters. CGNP clusters had an initial hydrodynamic diameter of 49.8 nm, which was increased to 52.4 nm after the conjugation of RGD peptides. The surcharge of ICG chromophore further increased the diameter to 56.0 nm. The presence of polyethylene glycol (PEG) on the surface of CGNP clusters-RGD was also confirmed using Fourier-transform infrared spectroscopy (FTIR) (Fig. S1E). The FTIR spectrum of CGNP clusters-RGD showed all characteristic peaks that could be found in PEG with molecular weight of 2000.

In vitro assessment of nanoparticles for PAM and OCT imaging.

To test the detection threshold of CGNP clusters-RGD for each modality, silicone tube phantoms containing CGNP clusters-RGD at different mass concentrations (i.e., 0 (saline), 0.005, 0.01, 0.02, 0.04, and 0.08 mg/mL) were imaged with PAM at 650 nm and OCT. Both PAM and OCT signal intensities were quantified using a region of interest (ROI) analysis as shown in (Fig. S2). It was shown that both PAM and OCT signal intensities were linearly correlated with the concentration of CGNP clusters-RGD ($p<0.001$, $R^2 = 0.99$ and 0.97, respectively) (Fig. 2E–F). The lowest detectable concentration of CGNP clusters-RGD

was approximately 0.01 mg/mL for both PAM and OCT imaging. To examine for potential photobleaching, the CGNP clusters-RGD were irradiated by 650 nm nanosecond laser at pulse repetition rate of 1 kHz with a fluence of 0.01 mJ/cm^2. During laser irradiation for 65,000 shots, the detected PAM intensities were stable and did not vary more than 2% (Fig. 2G). The blue line shows the average PA signal. To observe the optical absorption of CGNP clusters-RGD in biological environment, ARPE-19 cells were cultured with CGNP clusters-RGD at a final concentration of 100 μg/mL in media overnight to allow the cellular uptake of nanoparticles. Unlabeled ARPE-19 cells were used as control. The absorption spectra in Fig. 2H showed that CGNP clusters in ARPE-19 cells generated a broader absorption band compared to that of the colloidal solution of CGNP clusters (Fig. 2B) as a result of the accumulation of the CGNP clusters within the cells.

Biocompatibility and cytotoxicity of the CGNP clusters-RGD were tested using ARPE-19 cells to examine the effect of CGNP clusters-RGD on cell viability using MTT cell proliferation assay and flow cytometry analysis (see Supplementary Information). The cytotoxicity experiments demonstrated that after treatment with the CGNP clusters even at a high concentration of 100 μg/mL and long incubation time of 48 hrs, only minimal change on cell viability was induced with the cell survival rate higher than 80% (Figs. 2I–K, and Fig. S3A). Besides, cells under laser illumination at different laser fluences ranging from 0.0025 mJ/cm^2 to 0.08 mJ/cm^2 showed high survival rate and exhibited more than 80% cell viability. This implies that the used laser energy is safe without any severe photothermal effect on the cells (Fig. 3B). In addition, quantitative analysis measured by flow cytometry (Fig. 2L) showed that the percentage of living, apoptotic, and necrotic cells were 86.34%, 7.65%, and 6.01%, respectively, and cell viability was not different from a control group, illustrating that the cellular uptake of CGNP clusters-RGD did not lead to cytotoxicity. *In vivo* biosafety of CGNP clusters-RGD was also performed in mice using serum analysis to evaluate whether CGNP clusters-RGD could induce undesired side effects in living animals (See Supplementary Information). On day 90 after administration of CGNP clusters-RGD, mice serum analysis showed that each mouse had normal levels of alanine aminotransferase (ALT), blood urea nitrogen (BUN), creatinine (CREA), and alkaline phosphatase (ALP) (Supplementary Table S1), demonstrating no systemic, kidney, or liver toxicity.

Transmission electron microscopy (TEM), confocal laser scanning microscopy, and darkfield microscopy images confirmed successful labeling of ARPE-19 cells with CGNP clusters-RGD and ICG-CGNP clusters-RGD after incubation with them for different periods of time (day 1 and 4) at various concentrations ranging from 12.5 μg/mL to 100 μg/mL when compared with control (unlabeled) cells. All darkfield images (Figs. 2M–P) showed orange color due to intense light scattering in the 650 nm range determined by their peak absorption wavelength. Disassembly of CGNP clusters-RGD would have been indicated by a shift in color to green as shown in Fig. S3F–G. Figs. 2Q–R and Figs. S3C–H show the confocal laser scanning microscopy images of the treated cells. The results showed that CGNP clusters-RGD were located at lysosomes and stable within cells membrane since no significant changes were observed on fluorescence even at day 4. The TEM confirmed the internalized CGNP clusters-RGD inside the tissue (Fig. 2S–T). Figure 2U illustrates the TEM of the internalized CGNPs inside the ARPE-19 cells for 96 hrs. This image showed

that CGNP clusters were disassembled into discreet and small GNPs with the size less than 20 nm.

Furthermore, the quantity of CGNP clusters internalized into ARPE-19 cells was analyzed with inductively coupled plasma mass spectrometry (ICP-MS). As shown in Figs. 2V–W, the quantity of internalized CGNP clusters measured as Au mass/cell was linearly increased with the concentration of nanoparticles (Fig. 2V) and estimated to be 114 pg per cell after incubating ARPE-19 cells with CGNP clusters with concentration of 100 μg/mL for 24 hrs. This quantity increased to 190 pg when the incubation time was extended to 48 hrs (Fig. 2W). These results confirmed the highly efficient labeling of ARPE-19 cells with CGNP clusters, which would enable the use of both PAM and OCT for long-term cell tracking.

In order to track ARPE-19 cells for a long period using PAM and OCT, cells should be labeled with as many CGNP clusters as possible without impairing their function. This is because the number of the transplanted cells increases after every cell division, resulting in dilution of the labeled CGNP clusters inside cells and therefore reduced signal of PAM and OCT over time. The cellular uptake of CGNP clusters was concentration- and incubation time-dependent. As shown in confocal microscope images (Figs. 2N–P, Figs. 2Q–R, Figs. S3G–E, and Fig. S3L) and *in vitro* PAM images (Fig. 3A), the higher the incubation concentration of CGNP clusters, the more these clusters would be taken up into cells, providing stronger signal for both fluorescence and photoacoustic imaging.

To determine the optimal cell density threshold for subretinal injection *in vivo*, the PAM and OCT signals generated from the CGNP clusters -labeled ARPE-19 cells compared to that from unlabeled ARPE-19 cells were examined in tissue-mimicking agarose phantom studies. The tissue-mimicking agarose phantom containing fixed ARPE-19 cells at different concentrations ranging from 10^1 to 10^6 cells per microliter (N=3 per concentration) were imaged with PAM and OCT imaging. The PAM images acquired at 650 nm and the OCT images (B-scan and 3D) show stronger PAM and OCT signals from CGNP clusters-labeled ARPE-19 cells compared to that from unlabeled ARPE-19 cells (Fig. 3B–E). The measured signal amplitudes using ROI analysis show up to 32-fold increase in the mean photoacoustic signal (3.91±0.09 a.u. for 10^6 cells *vs* 0.12±0.02 (a.u.) for 0 cells), and 10-fold increase in the mean OCT signal of CGNP clusters-labeled ARPE-19 cells compared with unlabeled cells (Fig. 3F–G). At the lowest cell concentration, both PAM and OCT contrast were enhanced by up to 7-fold. These high PAM and OCT signal intensities were achieved from 10,000 cells, which is approximately 1,000 times below the clinically injected dose of stem cells, illustrating that the present method provides sufficient sensitivity to track progenitor cells in clinical applications[16,24].

Real-time OCT imaging-guided subretinal injection of transplanted cells.

After *in vitro* validation of the potential of our multimodality PAM and OCT imaging for tracking CGNP clusters-labeled ARPE-19 cells, the clinical procedure of progenitor cell transplantation into the subretinal space in the retina was implemented with the assistance of real-time OCT imaging guidance and followed by multi-modality imaging including color fundus photography, PAM, and indocyanine green (ICG) fluorescence imaging. Our group has previously reported the feasibility of using real-time OCT to guide subretinal injection

of VEGF and Matrigel[25]. As shown in Fig. S4 and supplementary video S1, and S2, the shaft of 33G needle was visualized and the needle tip reached the subretinal space without damage to the underlying choroidal vessels. The video shows the depth, needle orientation, and the real-time administration of cells delivered into the subretinal space. This real-time OCT imaging guidance allows one to adjust the injection trajectory and to improve injection accuracy for reducing the risk of retinal and choroidal vessel damage during subretinal injection.

Longitudinal *in vivo* PAM imaging of CGNP clusters-labeled ARPE-19 cells in rabbit eye with localized photocoagulation lesions.

Following successful delivery of CGNP clusters-labeled ARPE-19 cells at concentration of 10^6 cells/mL into the subretinal space of two different living rabbit models (with and without laser photocoagulation lesions), the distribution of these ARPE-19 cells in the subretinal space was mapped using color fundus photography, ICG fluorescence, PAM, and OCT. It was hypothesized that CGNP clusters-labeled ARPE-19 cells were distributed in the subretinal space, creating an initial PAM, OCT, and fluorescence signal illustrative of viable cells immediately post-injection. This initial PAM and OCT signal intensities were used to compare with the follow up PAM and OCT signal intensities to evaluate viability of the transplanted cells over time as well as their migration pattern. The transplanted ARPE-19 cells into the rabbit retina having localized RPE damage *via* photocoagulation lesions were visualized using PAM imaging at two different optical wavelengths of 578 nm to visualize vasculature and 650 nm to visualize ARPE-19 cells pre- and post-injection. Before subretinal injection of CGNP clusters-labeled ARPE-19 cells, two-dimensional (2D) and three-dimensional (3D) baseline PAM images of photocoagulation lesions were obtained on three rabbits (Fig. 4A). At 578 nm, the margin of laser lesions was clearly visible with high image contrast. These visualized PA signals primarily came from the hemoglobin (Hb) within retinal and choroidal vessels. In contrast, at 650 nm, minimal signal is detected without injection of labeled cells or after injection of unlabeled cells (Fig. S5) due to very low intrinsic PAM signal at the wavelength of 650 nm. After acquiring baseline images, 30 μL of CGNP clusters-labeled ARPE-19 cells at a concentration of 10^6 cells/mL were transplanted into the subretinal space with the aid of real-time OCT imaging guidance. Figures 4B show 2D and 3D PAM images obtained immediately post-injection. These images show the distribution of ARPE-19 cells to a depth of ~500 μm with excellent contrast against the adjacent retinal vasculature. Both anatomy of the retinal and choroidal vessels and ARPE-19 cells were observed in the PAM images acquired at 578 nm. In contrast, PAM images acquired at 650 nm show labeled ARPE-19 cells only. The high contrast at 650 nm is due to the little optical absorption of Hb and the strong optical absorption of CGNP clusters at that wavelength. Volumetric 3D data achieved from different excitation wavelengths were rendered and co-registered in the same orthogonal planes using Amira software without any post-image processing (see Supplementary Information). Longitudinal PAM imaging was performed on the same rabbit at different time points of 0, 1, 5, 7 days and up to 90-day post-injection to determine the feasibility of tracking the distribution and migration of the transplanted cells longitudinally over a long period. A representative selection of these images is displayed in Figures 4C–D. These images show that the transplanted cells were randomly distributed in the subretinal space at day 1 and started to migrate towards the

pre-induced photocoagulation lesions from day 2 and approached to the maximum on day 7. Whited dotted circles indicate the positions of the photocoagulation lesions and migrated cells. Note that the cell population was rapidly reduced from day 1 post-injection, which was possibly caused by cell death or migration out of the image plane. Using ROI analysis and image segmentation algorithm (see Supplementary Information and Fig. S6), the migration area of the transplanted ARPE-19 cells at day 1 was estimated to be 2.91±0.03 mm^2, which is 115% larger than that measured at day 0 (area=2.53±0.04 mm^2). The migration areas of ARPE-19 cells gradually reduced over time, revealing the gradual reduction of ARPE-19 cells.

Longitudinal *in vivo* PAM imaging of CGNP clusters-labeled ARPE-19 in rabbit eye without photocoagulation lesion.

To further examine the distribution and migration pattern of the transplanted cells, we performed experiments using a group of rabbits without pre-induced laser photocoagulation in the eye (N=3) for serving as a negative control. Figure 4E–H exhibits the *in vivo* longitudinal PAM tracking of the transplanted CGNP clusters-labeled ARPE-19 cells before and after subretinal injection (concentration=10^6 cells/mL, dose=30 μL) at different time points over a period of 90 days. These images show the location of cells with high spatial resolution and contrast. The PAM image contrast is higher at the injection site than the surrounding area (yellow arrows). The living cell population gradually decreased over time and was undetectable by day 70. The ARPE-19 cells were found at the injection site and randomly distributed in the subretinal space with dynamic changes over time. Image segmentation was employed to identify the margin of the cell migration and the area dominated by the cells was measured for each interval (Fig. S6A–B). The data exhibits that the migration area varied from 171.31±0.08 mm^2 to 14.59±0.10 mm^2 over a period of 56 days, demonstrating the capability of PAM for monitoring cell population growth and migration over time. The imaging results in Fig. 4 show distinctive distribution patterns of progenitor cells, i.e., concentrated at lesion areas in rabbit eyes with pre-induced photocoagulation lesions or randomly in rabbit eyes without pre-induced photocoagulation lesions. Thus, labeled by CGNP clusters, the populations and distribution of the ARPE-19 cells in the retina can be longitudinally evaluated by our imaging system.

In vivo kinetic evaluation of CGNP clusters-RGD.

The time-dependent photoacoustic signals from free CGNP clusters-RGD (not within ARPE-19 cells) after subretinal injection were assessed to evaluate the lifetime of these nanoparticle *in vivo*. One could hypothesize that CGNP clusters could be released from cells, and they could stay locally in the subretinal space, resulting in inaccurate imaging assessment of the ARPE-19 cell population. Figure 5A–D illustrates longitudinal assessment of subretinal injection of free CGNP clusters-RGD. In this experiment, a group of rabbits (N=3) received subretinal injection of 30 μL CGNP clusters-RGD at a concentration of 20 μg/mL were imaged at different time points over 90 days post-injection. The PAM image acquired immediately after the injection (day 0) at 578 nm shows the injection area with no image contrast in comparison to the surrounding tissue because of the retinal detachment at this area induced by injection. When the subretinal fluid in the detachment area was absorbed, the morphology of retinal and choroidal vessels was clearly visualized in the PAM

images (from day 7 to day 90). Also due to the detachment, minimal contrast was observed in the PAM image obtained at 650 nm on day 0 post-injection; whereas high image contrast was observed in the PAM image acquired on day 7 after the subretinal fluid was absorbed. The image contrast at 650 nm was then gradually reduced from day 14 and completely cleared by day 21. This rapid decline in PAM signal from subretinally injected free CGNP clusters-RGD by day 21 contrasts with the persistent PAM signal from subretinally injected CGNP clusters-RGD labelled ARPE-19 cells which lasted for at least 90 days. This result in Fig. 5 also indicates that free CGNP clusters-RGD will be rapidly cleared from the subretinal space when they are not inside cells.

Longitudinal quantification of PAM signal generated from CGNP clusters-labeled ARPE-19 cells.

To determine the contrast enhancement by the CGNP clusters-labeled cells transplanted into the subretinal space against the surrounding microvasculature, we quantified the PAM signals in the ROIs (white rectangles) around the injection area and along the migration pattern (Fig. S6 C–D). Figure 5E shows the quantification of PAM signals produced at each time point after subretinal injection of either CGNP clusters-RGD-labeled cells (with and without localized laser injury) or free CGNP clusters-RGD, serving as the negative control. For the group with laser injury in the retina (blue line), enhanced by the CGNP clusters inside cells, the PAM signal increased by 31-fold, from a pre-injection value of 0.12±0.01 (a.u.) to a post-injection value of 3.72±0.18 (a.u.) (p=0.001). The PAM signal remained high up to 56 days and then gradually declined. Similarly, for the group without laser injury in the retina (red line), the PAM signal, enhanced by the CGNP clusters inside cells, increased by 31-fold, from 0.13±0.01 (a.u.) for pre-injection to 3.96±0.1 (a.u.) for post-injection (p=0.001). The PAM signal gradually decreased and still achieved strong PA signal up to 56 days post injection. These results confirmed the stability of CGNP clusters internalized by the ARPE-19 cells, suggesting the minimal leakage of CGNP clusters from the ARPE-19 cells during their *in vivo* migration. In contrast, for the control group injected with free CGNP clusters-RGD (black line), the PAM signal approached to the maximum on day 7, increasing from 0.12±0.01 (a.u.) for pre-injection to 2.92±0.03 (a.u.) for post-injection, and then rapidly reduced by day 21.

To determine the potential photobleaching of CGNP clusters *in vivo*, PAM images were acquired three times from the same scanning area and the PAM signal were determined using ROI analysis. The imaging result in Fig. S7 shows that PAM signal fluctuated within a small range of 1.74%, from 3.49±0.29 (a.u.) to 3.43±0.0.40 (a.u.) over three scans. This result suggests that the CGNP clusters internalized by cells were stable over the multiple scans at the utilized laser fluence. Spectroscopic PAM images were also acquired with the excitation wavelengths ranging from 510 nm to 710 nm (Fig. S8). The quantitative spectroscopic result shows the peak PAM signal at 650 nm, which is consistent with the absorption spectrum of CGNP clusters measured *ex vivo* (Fig. 2H). This result confirmed the excellent biostability and photostability of the CGNP clusters again.

In vivo tracking the migration of transplanted ARPE-19 cells to sites of laser-induced RPE injury with OCT imaging.

Real-time OCT imaging was performed to guide subretinal injection of CGNP clusters-labeled ARPE-19 cells into the subretinal space (Supplementary Video S2 and S3). Immediately after injection, OCT imaging was used to continuously monitor the distribution and migration of the transplanted cells at different time points. 2D view B-scan OCT images overlaid with MIP PAM images revealed the distribution of the cells over time (Figure 6). B-scan OCT image acquired pre-injection showed the different retinal layers, including the choroid, RPE, internal limiting membrane (ILM), ganglion cell layer (GCL), inner plexiform layer (IPL), inner nuclear layer (INL), outer plexiform layer (OPL), outer nuclear layer (ONL), external limiting membrane (ELM), and photoreceptors which are consistent with retinal histology (Fig. 8A). Laser lesions were clearly observed (red arrows), resulting in full thickness hyper-reflective retinal changes. Figure 6B presents a B-scan OCT image acquired immediately post-injection, showing that CGNP clusters-labeled ARPE-19 cells (green arrows) were clearly observed within the subretinal space with an excellent contrast at a depth between 200 and 600 μm since these cells could be distinguished from both RPE (yellow arrows) and subretinal fluid (white dotted arrow) because of strong optical scattering from the internalized CGNP clusters. Long-term longitudinal visualization of the viability, state, and location of the transplanted cells labeled with CGNP clusters were obtained with OCT over a period of 90 days (Figure 6B–J), which indicated the presence of these cells at the sites of laser injury in the subretinal space (yellow arrows). The MIP PAM images were co-registered with the B-scan OCT images, showing great co-localization between the two modalities. To quantify the contrast originating from the transplanted cells, semiautomatic image segmentation was implemented to extract ARPE-19 transplanted cells using Amira. The spectral contrasts were determined (Fig. 6K). The OCT signal showed a 14% reduction from its initial value at 15 min post-injection compared with that of pre-injection, which could be due to light attenuation caused by subretinal fluid after the injection. Following this slight drop, the OCT signal rapidly increased to 180% compared to that of pre-injection. This signal then gradually decreased thereafter.

In vivo triple-modality visualization of CGNP clusters-labeled ARPE-19 cells.

To further verify the distribution of transplanted cells after subretinal injection, fluorescence microscopy was performed along with PAM and OCT imaging. Indocyanine green (ICG) (Ex=789 nm, Em=814 nm) was selected as a fluorescent contrast agent and conjugated onto the surface of functional CGNP clusters-RGD (i.e. ICG@CGNP clusters-RGD). After incubating ARPE-19 cells with ICG@CGNP clusters-RGD at a concentration of 100 μg/mL for 24 hrs, these labeled cells were delivered into the subretinal space. ICG fluorescence, PAM, and OCT imaging were conducted consecutively on rabbits pre- and post-injection for up to 90 days (Fig. 7, and Fig. S9). The transplanted cells were clearly visualized post-injection for all 3 imaging modalities (ICG fluorescence, PAM, and OCT). PAM images at 650 nm were co-registered in orthogonal planes, which allowed improved visualization of the state, distribution, and migration of the cells. Fluorescence intensity and distribution areas were estimated and plotted as shown in Fig. S9E. The normalized fluorescence intensity increased by 39-fold post-injection. The signal remained unchanged over a period of 5 days and then rapidly decreased afterward. ICG fluorescence signal nearly resolved by

day 28 post-injection. This might result from ICG dye degradation or photo-bleaching. The decrease of fluorescence signal was significantly faster than that of PAM signal, indicating that ICG fluorescence can label and track ARPE-19 cells *in vivo* only effectively in a short term, whereas PAM imaging allows for longitudinal tracking of ARPE-19 cells *in vivo* over a much longer duration for improved monitoring of cell therapies.

Histological validation of tissue after cell transplantation.

All the rabbits used for the experiments described above were euthanized at day 90 for histological analysis. Histological analysis was employed using standard hematoxylin and eosin (H&E) stain. The H&E images from four different treatment groups provided additional information about cell viability and migration pattern in the subretinal space (Figs. 8A–J). There were significant changes in the RPE layer with and without laser injury after subretinal injection of unlabeled ARPE-19 cells and CGNPs labeled ARPE-19 cells. The RPE layer after laser photocoagulation and cell injection (Fig. 8C–E and Fig. 8H–J) is thicker than that of both control (Fig. 8A,F) and laser injury without cell injection (Fig. 8B,G). For example, after the subretinal injection of ARPE-19 cells, the thicknesses of the RPE layer with and without laser injury was measured to be 376.69±16.75 μm and 109.79±10.20 μm (green dotted arrows), respectively, while the thicknesses of RPE layers in control tissues and laser injured tissues without cell injection were 17.72±0.48 μm and 16.40±4.10 μm, respectively. In the model of laser photocoagulation followed by subretinal injection of transplanted cells, cell migration and growth at the lesion sites (Fig. 8J) was higher than that in the areas without laser lesions (Figs. 8H, I). By using Imaris software to determine cell proliferation, the cell populations were estimated to be 61,406 cells per mm^2, 5-fold higher than cell populations in tissues without photocoagulation treatment (P_{cells} = 13,082 cells per mm^2). These results illustrate that transplanted cells helped to regenerate and replace damaged or lost RPE cells. In addition, the position of laser injuries was clearly visualized (red arrows), showing disorganization of the RPE layer (yellow arrows) (Figs. 8G). The tissue after laser photocoagulation showed full thickness changes in the retinal structure and loss of the inner plexiform layer (red arrow). In contrast, histological images of control tissue (Fig. 8A,F) showed normal cellular morphology and nuclei, and the retinal layers such as RPE, Bruch's membrane, and choriocapillaris. This histological image matches well with B-scan OCT images (Fig. 6A).

To further visualize donor human ARPE-19 cells, immunohistochemistry was performed using an antibody staining against RPE65 (Figs. 8K–O). Nonpigmented RPE from the transplanted ARPE-19 cells was overall strongly positive for RPE65 (red fluorescent color) (Figs. 8M–O). DAPI was used to stain cell nuclei, which appeared blue under fluorescence microscopy. RPE65 immunoreactivity confirmed the presence of ARPE-19 cells. The ARPE-19 cells were effectively joined and overlapped with well-preserved photoreceptor nuclei and outer segments in both tissue with and without laser injury. These findings demonstrated that the subretinal injection of ARPE-19 can properly integrate and regenerate the monolayer of RPE to replace lost RPE after photocoagulation and injury. To confirm the ability of PAM and OCT to detect RPE loss and regeneration at laser injury sites, the MIP PAM and B-scan OCT images were correlated with histological images (Fig. 9). As shown in the overlay image (Fig. 9D), ARPE-19 cells migrated to laser injured sites. None

were present in the surrounding retinal tissues. Biosafety was also evaluated for all treatment groups. TUNEL assay data showed no evidence of apoptotic cells in eyes tissues and organs, confirming the use of CGNP clusters was safe (Fig. 10 and Fig. S10)

This study demonstrates long-term, non-invasive longitudinal tracking of progenitor cells *in vivo* with high spatial resolution in large animal eyes using multimodality PAM and OCT imaging coupled with CGNP clusters. The benefits of this technique are highlighted by a number of features. First, the fabricated CGNP clusters have a red-shifted absorption peak at 650 nm and meanwhile still maintain a small size, allowing for enhancing both PAM and OCT signal in a window with low background signal from endogenous tissues. Second, this multimodality PAM and OCT imaging system with high spatial resolution allows for real-time guidance of delivering progenitor cells into the retina in large animal eyes and longitudinal mapping the cells in 3D with histological resolution of the retinal layer in which the cells are located.

Recently, GNPs with different sizes and shapes have been investigated as promising contrast agents for *in vivo* noninvasive tracking stem cells/progenitor cells[15,17]. However, the applied nanomaterials may affect the cells, including viability after transplantation, influence on cell migration, differentiation, engraftment, and possible long-term cytotoxicity. The cytotoxicity of GNPs on cells may depend on particular characteristics of GNPs such as surface reactivity, degradation or ion leaching, GNP agglomeration, and sedimentation[26,27]. Thus, any GNPs used for cell tracking should demonstrate biocompatibility and biostability. The fabricated CGNP clusters utilized in this study have several specific properties. *Via* assembling GNP monomers with diameter of 20 nm into CGNP clusters, the UV-Vis absorption peak was red-shifted from 520 nm to 650 nm. This represents an important advantage in terms of less toxicity and improved biocompatibility over other GNP structures which achieve red-shifted absorption peak in the red region by increasing nanostructure size. Furthermore, this nanoparticle cluster-based contrast agent demonstrates excellent biostability *in vitro* and *in vivo* and great photostability under the laser fluence required for PAM imaging. Our experiments showed that the synthesized CGNP clusters were nontoxic to human ARPE-19 cells. Their optical properties did not change under nanosecond pulsed laser illumination during PAM and the internalized CGNP clusters were stable for up to 3 months in cells. Transplanted cells labeled with CGNP clusters in the subretinal space led to a 30-fold increase in PAM signal compared to that acquired pre-injection, demonstrating the capability of PAM in combination with OCT for tracking progenitor cells *in vivo* in a longitudinal fashion.

Due to the remarkable capability of evaluating and monitoring the location, distribution, and migration of cells in 3D, our multimodality imaging system permits for accurate visualization of the fate of cells after transplantation. Also, the *in vivo* experiments showed that because of the high labeling efficiency, the CGNP clusters internalized by the cells provided stable PAM signal for up to 56 days, making it possible to repeatedly image the transplanted cells throughout that time. The prolonged high PAM image contrast demonstrated by these results indicated that PAM imaging of CGNP clusters-labeled ARPE-19 cells allowed for estimating the population of cells migrated to the injured sites and long-term longitudinal tracking the regenerative cell-based therapies. Although

fluorescent dyes can also be used for cell labelling to enable fluorescence imaging based *in vivo* cell tracking, fluorescent dyes suffer from poor biostability and photostability. As shown in our experiment, ICG fluorescence imaging was able to track the cells for up to 7 days only, much shorter than the duration achieved by PAM imaging in the same experiment. This finding is consistent with previous studies using quantum dots for labeling and tracking endothelial progenitor cells[28]. The decrease in fluorescence emission efficiency may be caused by biodegradation or photobleaching effects during longitudinal imaging sessions.

Furthermore, our study demonstrates that the utilized CGNP clusters are not cytotoxic, and cells labelled with these clusters do not induce any immune response or disruption of retinal function after injection in the subretinal space. The use of nanosecond pulsed laser to excite the internalized CGNP clusters for inducing PAM signals has also been shown not to be cytotoxic or triggering an immune response[29]. In our study, the excitation laser fluence used in PAM (~0.01 mJ/cm^2 at 578 and 650 nm) was kept to be only half of the American National Standards Institute (ANSI) limit of the maximum permissible single laser pulse fluence on the retina (i.e., 0.02 mJ/cm^2 at 578 and 650 nm)[23,30,31,32]. Another important aspect to be considered for imaging is acquisition time. Long acquisition time may affect the image resolution, motion artifacts, image quality, and possibly the graft cell function and viability as described by Organisciak *et al.* and Robinson *et al.*[32,33]. In this study, volumetric PAM imaging can be achieved with a high spatial resolution over a field of view of 4×4 mm^2 in less than one minute. The acquisition time is limited by the laser repetition rate of 1 KHz of our nanosecond laser (NT-242, Ekspla, Lithuania), and can be further reduced *via* using pulsed lasers with higher repetition rate that are commercially available[34].

Stem cell-based RMTs are promising treatment techniques for future clinical applications to treat numerous currently incurable diseases. However, there remain several important challenges before translating this technique to the clinic. One of them is to understand the distribution, migration, and viability of the transplanted stem cells in complex biological environments. The capability to perform accurate, non-invasive, and real-time image tracking of transplanted cells *in vivo* with cellular level sensitivity and spatial resolution could shed new light on both research and clinical applications of stem cell-based RMTs. The current study presents a high spatial resolution, 3D PAM and OCT multimodality imaging system powered by an ultrapure, biocompatible, and photostable CGNP clusters serving as the contrast agent for longitudinally tracking migration of progenitor cells within the subretinal space over an extensive period of time (3 months) in large animal eyes (rabbits) *in vivo*. The fabricated CGNP clusters exhibit a red-shifted absorption peak at 650 nm which make them ideally suitable to track cell fate in biological tissues *in vivo*. Because of their high labelling efficiency, excellent colloidal stability in physiological/ biological environments, and exceptional photostability under nanosecond pulsed laser illumination, CGNP clusters provide a stable PAM signal for more than 3 months, which is an essential requirement for longitudinal imaging and tracking cells over an extended time period.

Conclusions

This study has demonstrated that human ARPE-19 cells can be successfully labeled with CGNP clusters. These labeled cells can be monitored in real-time during injection into the subretinal space using OCT, and the internalized CGNP clusters can provide excellent PAM signals above background to differentiate the transplanted cells from microvasculature. Moreover, *via* co-registration of PAM images having high spatial resolution with OCT images offering accurate retinal anatomical information, the exact retinal layer in which the transplanted ARPE-19 cells are located can be determined throughout the entire tracking period of 3 months. Therefore, the PAM and OCT multimodality imaging system presented in this study allows for long-term, non-invasive, and real-time tracking the transplanted progenitor cells *in vivo* in the subretinal space with information of the identified retinal anatomy layers. This technology can lead towards improved RMTs by providing better understanding the location, migration, and distribution of stem cells.

Materials and Methods

Synthesis of CGNP clusters-RGD:

RGD functionalized CGNP clusters (CGNPs-RGD) were synthesized as a great exogenous contrast agent for cell labeling and tracking using high resolution multi-modality PAM and OCT imaging. A detailed synthesis and characterization of CGNP clusters-RGD was described in our previous study.[35] Briefly, ultrapure GNP monomers were fabricated using the ytterbium-doped femtosecond fiber laser (FCPA μJewel D-1000, IMRA America, Ann Arbor, MI) (see Supplementary Information) to be naturally negatively charged. There are no capping agents or stabilizing ligands required to maintain their stability. Pentapeptide with an amino acid sequence of CALNN and cysteamine ligands were used to assemble discreet GNP monomers into CGNP clusters. Briefly, discrete GNP monomers (d_{avg} = 20 nm) were mixed with CALNN peptides at a defined molar ratio of 2000:1 between CALNN peptides and GNP monomers and kept at room temperature (RT) for 2 hrs (CALNN@GNPs). The surface of CALNN@GNPs was then mixed with cysteamine molecules with a molar ratio of 1700:1 between cysteamine molecules and CALNN@GNPs and kept at RT for 24 hrs or several days until CGNP clusters structure was completed by assessing the color change from red-pink to blue.

The raw CGNP clusters were then functionalized with RGD ligand as described in our previous work[36]. 5 mL CGNP clusters at OD 10 were PEGylated by adding 20 μL thiol-terminated PEG (PEG-SH) with molar mass of 2000 g mol^{-1} (PEG 2k-SH) having concentration of 1 mM and kept at RT for 2 hrs. After the reaction, 60 μL RGD peptide solution at a concentration of 1 mM was added to partially PEGylated CGNP clusters and the mixture was kept at room temperature for an additional 2 hrs. Then, the mixture was centrifuged at 1000 g for 30 min. Final optical density at 650 nm (absorption peak wavelength) of the CGNP clustes-RGD was adjusted to ~100 by resuspending the pellet with 4 mM borate buffer (pH 8.2) containing 5 mg/mL BSA after removing the supernatant.

CGNP clusters-RGD were further coated with indocyanine green (ICG) as a near-infrared fluorescent nanoconjugates to allow for triple fluorescence, PAM, and OCT imaging. CGNP

clusters were mixed with PEG 2k-SH and kept undisturbed for 2 hrs at room temperature. Then, partially PEGylated CGNP clusters were labeled with ICG dye by adding to them 50 μL aqueous solution of ICG-PEG 2k-SH with concentration of 1 mM. This mixture was kept undisturbed for 2 hrs to ensure sufficient ICG labeling (ICG@CGNP clusters). Afterwards, 70 μL RGD solution with concentration of 1 mM was added to the ICG@CGNP clusters. The resultant solution was allowed to stand for additional 2 hrs at room temperature to enable the conjugation of RGD peptides onto unoccupied space of the CGNP clusters. After this reaction, the final solution was transferred into a 15 mL centrifugal tube and was spun down at 1000 g for 0.5 hour to a pellet. The final OD of the colloidal solution of PEGylated and RGD peptide-conjugated CGNP clusters labeled with ICG dye (ICG@CGNP clusters-RGD) was adjusted to ~10 at 650 nm by resuspending the pellet with 4 mM borate buffer (pH 8.2) containing 5 mg/ml BSA after removing the supernatant.

Physical and optical characterization of CGNP clusters-RGD:

The particle morphology, size distribution, and optical absorption spectrum were performed to evaluate successful synthesis. Dynamic light scattering (DLS) method was used to assess hydrodynamic particle size distribution of the CGNP clusters (Zetasizer Nano ZS90, Malvern Instruments, Malvern, Worcestershire, UK). Transmission electron microscopy (TEM) was performed to evaluate the particle morphology (JEOL 2010F, Japan). The absorbance spectrum was determined from 350 nm to 800 nm using a spectrophotometer (UV-3600, Shimadzu Corp., Japan). The infrared spectra of PEG 2k-SH, ICG, CGNP clusters, CGNP clusters-RGD, and ICG@CGNP clusters-RGD were analyzed using a PerkinElmer spectrum 100 FTIR spectrometer (PerkinElmer Inc., Waltham, MA) equipped with an attenuated total reflection (ATR) diamond. (see Supplementary Information). The stability of the synthesized CGNP clusters was assessed by measuring the optical absorbance at various times up to 2 months. The biological stability of CGNP clusters was also evaluated in cells. CGNP clusters were incubated with ARPE-19 cells for different times (1 day and 4 days). The biodistribution of CGNP clusters was observed using confocal microscopy. In addition, the optical absorption spectrum of the treated cells was also measured using spectrometry. (see Supplementary Information). To evaluate the photostability of the CGNP clusters, the sample was irradiated with 650 nm nanosecond pulsed laser at different fluences of 0.005, 0.01, 0.02, and 0.04 mJ/cm^2. The photostability of CGNP clusters was further evaluated through *in vitro* PAM imaging. The PAM image of fixed cell samples was acquired 4 times at the same position, and PA signal amplitudes were measured (see Supplementary Information).

Cell Culture:

A human retinal pigment epithelial cell line with differentiated properties (ARPE-19) were generously donated by Dr. David Antonetti at the University of Michigan. ARPE-19 cells were grown in DMEM/F12 medium supplemented with L-glutamine, 15 mM HEPEs (Sigma, St. Louis, MO, USA), 1.16 g/L sodium biocarbonate, 10% fetal bovine serum, and antibiotic-antimycotic. Cells were maintained in a humidified incubator at 37 ^{o}C in the presence of 5% CO_2.

In vitro toxicity and cellular uptake of CGNP clusters-RGD:

The amount of CGNP clusters taken up by cells were monitored and evaluated. Ultrapure colloidal solution of CGNP clusters-RGD was sterilized under UV light for at least 12 h prior to cell experiments. A sample of CGNP clusters-RGD were further conjugated with the fluorophore indocyanine green (ICG) for cell labeling analysis using confocal fluorescence microscopy analysis. The cells were incubated with CGNP clusters-RGD at different concentrations (0 (control), 25, 50, 100 μg/mL) for 24h and stained with FITC, DAPI, and PI (see Supplementary Information). Confocal fluorescence microscope, light scattering dark-field, and PAM images were acquired to examine the distribution of CGNP clusters. The cells with a density of 5×10^4 cells were cultured in 22 mm^2 cell culture plate with an open glass at the bottom for 24 hrs. Then, the cells were treated with ICG@CGNPs-RGD at a final concentration of 100 μg/mL in media and incubated for further 24 hrs. Afterwards, the cell media was replaced by fresh media containing lysotracker (LysoTracker™ Red DND-99, Catalog number: L7528, Invitrogen, Cålsbad, CA, USA) at final concentration of 1 μg/mL in media and incubated for 20 min in dark area. 1mL of 2.5% glutaraldehyde in 0.1M sodium cacodylate buffer were added into the treated cells and kept in room temperature for 20 min. Lastly, the sample stained with Alexa Fluor 488 phalloidin and DAPI (2.5 μL of phalloidin in 100 μL of formaldehyde and DAPI (100 μg/mL)). The samples were images using SP5 confocal laser scanning microscope (Leica, IL, USA). To quantitatively determine the amount of internalized CGNP clusters by each individual cell, the treated cells were collected, diluted in HCl and HNO3 acids, filtered, and then quantified using ICP-MS method (See Supplementary Information)

To examine the potential cytotoxicity of CGNP clusters to ARPE-19 cells, MTT assay was conducted. ARPE-19 cells were incubated with CGNP clusters at various concentrations from 12.5 to 500 μg/mL for 24 hrs and 48 hrs. Cell survival populations were determined using MTT assay methods (see Supplementary Information). To further quantify potential apoptosis, cell viability, and cell death, flow cytometry analysis was performed. The cells were incubated with 100 μg/mL of CGNP clusters for 24 hrs and 48 hrs. The media containing CGNP clusters were aspirated, and cells were harvested using Trypsin EDTA, stained with BD Annexin V-FITC apoptotic kit, and resuspended in PBS for flow cytometry analysis (see Supplementary Information).

Labeling of ARPE-19 cells with CGNP clusters-RGD for *in vivo* subretinal injection:

ARPE-19 cells were incubated with CGNP clusters-RGD at a final concentration of 100 μg/mL for 24 hrs. Then, cells were washed with cold phosphate buffer saline (PBS) three times to aspirate free CGNP clusters-RGD. 0.05% Trypsin/EDTA was used to harvest the CGNP clusters-labeled ARPE-19 cells. The harvested cells were centrifuged, counted, and resuspended in PBS (see Supplementary Information).

PAM and OCT imaging of CGNP clusters-labeled ARPE-19 cells *in vitro:*

Single cell detection using PAM imaging presented in Fig. 1a was achieved by imaging cover glass samples of cells incubated with CGNP clusters at different concentrations (0 (control), 25, 50, 100 μg/mL). Each sample was scanned at an area of 0.2 × 0.2 mm^2 at 650 nm with the laser fluence of ~0.003 mJ/cm^2. To examine the limitation of CGNP

clusters-labeled ARPE cells for *in vivo* PAM and OCT imaging, fixed cells labeled with CGNP clusters at 4 different concentrations of 0 (control), 25, 50, and 100 μL were used for phantom experiment. 10^6 cells/mL were mixed with 2% gelatin solution and poured into a phantom mold (see Supplementary Information). The phantom sample was imaged with the PAM and OCT imaging system. The minimum cell detectable density displayed in Fig. 3B was obtained by imaging a group of tube phantoms filled with six different amounts of ARPE-19 cells: 10^1, 10^4, 10^5, and 10^6 cells. The average of the PAM amplitudes above the background level *versus* amount of cells was measured and plotted in Fig. 3F.

Biodistribution and toxicity of CGNP clusters-RGD:

The body weight of all treated and untreated groups was recorded daily for 90 days. At day 90 post-cell injection, blood samples were collected for serum analysis and all rabbits were euthanized. Organs such as eye, heart, liver, lung, kidney, and spleen were extracted to measure the amount of gold accumulated in organs by ICP-MS (see Supplementary Information). Standard histological analysis using H&E staining and TUNEL assay were performed to assess the regeneration of damaged retina and potential apoptosis of CGNP clusters-labeled cells (see Supplementary Information).

Multi-modality high spatial resolution PAM, OCT, and fluorescence imaging and *in vitro* and *in vivo* experiments:

In vivo PAM and OCT images were achieved using a multi-modality, high spatial resolution imaging system (Figure 1a). The detail was described in previous studies[18,21,23,37] and in the Supplementary Information. All animal experiments were implemented in accordance with the instruction of the Association for Research in Vision and Ophthalmology (ARVO) Statement on the care and use of laboratory animals in Ophthalmic and Vision Research after the protocol was approved by the Institutional Animal Care and Use Committee (IACUC) at the University of Michigan (PRO00008566) and the Institutional Biosafety Committee (IBCA00001129).

New Zealand White rabbits (2.4–3.4 kg; 2–4 months old) were generously donated from the Center for Advanced Models and Translational Sciences and Therapeutics (CAMTraST) at the University of Michigan Medical School. Rabbits (N=21) were randomly divided into 7 groups: control group (subretinal injection of balanced salt solution (BSS)), subretinal injection of CGNP clusters-RGD, subretinal injection of ARPE-19 cells labeled with CGNP clusters-RGD, subretinal injection of ARPE-19 cells labeled with CGNP clusters-RGD conjugated with ICG, subretinal injection of ARPE-19 cells labeled with CGNP clusters-RGD following laser-induce RPE damage, laser-induced RPE injury group, and subretinal injection of unlabeled ARPE-19 cells (see Supplementary Information).

At day 4 following laser irradiation damage, retinal detachment resolved. All rabbit models were anesthetized with xylazine and ketamine and received subretinal injection of 30 μL labeled cells at a concentration of 10^6 cells per microliter. During the subretinal injection, real-time OCT imaging was used to guide the injection as described by our group previously[25]. Transplanted cells were then imaged with multi-modality imaging, including color fundus photography, fluorescence imaging, ICG fluorescence, PAM, and

OCT to visualize the distribution and migration of the transplanted cells and to assess the morphology of the retinal blood vessels. The rabbit's eyes were positioned at the center of the scan area, and the rabbit's bodies were placed on another stabilization platform to minimize motion artifact. BSS was applied on the eye surface every minute to provide acoustic coupling between the conjunctiva and the ultrasound transducer. A water circulating heating blanket was placed under the rabbit to keep the body temperature stable. Isoflurane 0.75% and oxygen (1 L/min) were provided to sustain anesthesia throughout the experiments. Respiration rate, heartbeat, and rectal body temperature were monitored. 1% tropicamide ophthalmic and 2.5% phenylephrine hydrochloride solution were used to dilate the pupils of the rabbits. Five minutes before the imaging session, 0.5% topical tetracaine was instilled in the eye for topical anesthesia, and lubricant was used to prevent dehydration of the cornea.

In PAM imaging, the spot size of excitation laser has a diameter of approximate 2 mm, and the fluence on the retina was ~80 nJ at 570 nm, which is half of the American National Standards Institute safe limit for the eye[23]. The maximum scan area was 5×5 mm^2 with 256×256 pixels. The image acquisition time was approximately 65 s and limited by the 1 kHz pulse repetition rate of our tunable OPO laser (NT-242, Ekspla, Lithuania). A custom-made needle-shaped ultrasound transducer with a central frequency of 27.0 MHz was used to detect the laser-induced acoustic signals. The axial and lateral resolutions were 37.0 and 4.1 μm, respectively. The PAM image data obtained at two wavelengths was aligned, reconstructed, and segmented in 3D using Amira software (Visualization Sciences Group). The average PAM signal within transplanted cells was measured for each PAM image. Error bars exhibit the standard deviation of measurements achieved in three different samples.

Spectral-domain OCT images were acquired by a commercially available OCT system (Ganymede-II-HR, Thorlabs, Newton, NJ) with modification. Briefly, the ocular lens after the scan lens and a dispersion compensation glass in the reference arm were added into the system[23,38]. The OCT excitation beam incident was coaxially aligned with the PAM excitation beam incident. Thus, OCT can be used to guide and help interpret PAM results. The lateral and axial resolutions of OCT are 4 μm and 3 μm, respectively. The average OCT, PAM, and fluorescence signal within transplanted cells was measured for each OCT, PAM and fluorescence image. Error bars exhibit the standard deviation of measurements achieved in three different samples.

Immunostaining and electron microscopy analysis:

To evaluate the interaction of the transplanted ARPE-19 cells with native cells after subretinal injection, immunohistochemistry staining was obtained with two different antibodies: primary RPE65 antibodies, secondary Alexa Fluor 555 donkey anti-rabbit IgG, and Alexa Fluor 647 donkey anti-mouse IgG antibodies. See the Supporting Information for further details. These slides were mounted with prolong gold mounting medium with DAPI (Vector Laboratories, Burlingame, CA, USA) using a 24×50 mm cover slip. The slides were observed using light Leica microscope (DM6000, Leica Biosystems, Nussloch, Germany) and images were digitally captured using Leica Application Suite software (LAS X, Leica

Biosystems, Nussloch, Germany). Post image processing and analysis were implemented using ImageJ and Imaris software.

For transmission electron microscopy (TEM) analysis, cells samples and liver specimens were evaluated to confirm the stability of CGNP clusters in biological tissues (See the Supporting Information for further details). TEM images were acquired using JOL-JEM 1400 Plus equipment (Japan Electron Optic, Tokyo, Japan).

Statistical methods:

A random-effects regression model was used to compare the control group without injection of ARPE-19 cells with the treated groups with injection of CGNP cluters-labeled ARPE-19 cells. All the experiments were performed at least three times. The student's t-test was implemented to evaluate any significant difference in image contrast between pre- and post-transplantation. The final data points were displayed as the average ± standard deviation (SD). A p-values of < 0.05 was used as statistically significant.

Supplementary Material

Refer to Web version on PubMed Central for supplementary material.

Acknowledgments

We would like to acknowledge the National Eye Institute and Fight for Sight- International Retinal Research Foundation for their generous financial support (grant number: YMP:1K08EY027458 and YMP: FFSGIA16002). This project was also funded by unrestricted departmental support from Research to Prevent Blindness, and the University of Michigan Department of Ophthalmology and Visual Sciences. This work utilized the Core Center for Vision Research funded by the National Eye Institute (P30 EY007003). We would like to thank Dr. David A. Antonetti for providing a human retinal pigment epithelial cell line with differentiated properties (ARPE-19), Dr. Xuen Liu and Dr. Qitao Zhang for assistance with the tissue culture and visualization of cell data using confocal laser microscope. The authors thank Dr. Thomas for assistance with immunohistochemistry. We thank Dr. Yuqing Chen and the University of Michigan CAMTraST for the generous donation of New Zealand white rabbits.

References

1. Huang Z; Xu J; Chen J; Chen H; Wang H; Huang Z; Chen Y; Lu X; Lu F;Hu J. Photoacoustic Stimulation Promotes the Osteogenic Differentiation of Bone Mesenchymal Stem Cells to Enhance the Repair of Bone Defect. Sci. Rep 7, 1–14 (2017). [PubMed: 28127051]
2. Jenq RR;Van den Brink MR Allogeneic Haematopoietic Stem Cell Transplantation: Individualized Stem Cell and Immune Therapy of Cancer. Nat. Rev. Cancer 10, 213–221 (2010). [PubMed: 20168320]
3. Vagnozzi RJ; Maillet M; Sargent MA; Khalil H; Johansen AKZ; Schwanekamp JA; York AJ; Huang V; Nahrendorf M;Sadayappan S. An Acute Immune Response Underlies the Benefit of Cardiac Stem Cell Therapy. Nature 577, 405–409 (2020). [PubMed: 31775156]
4. Garber K. RIKEN suspends first clinical trial involving induced pluripotent stem cells. Nature, 890–891 (2015).
5. Russell S; Bennett J; Wellman JA; Chung DC; Yu Z-F; Tillman A; Wittes J; Pappas J; Elci O;McCague S. Efficacy and Safety of Voretigene Neparvovec (Aav2-Hrpe65v2) in Patients with Rpe65-Mediated Inherited Retinal Dystrophy: A Randomised, Controlled, Open-Label, Phase 3 Trial. The Lancet 390, 849–860 (2017).
6. Falkner-Radler CI; Krebs I; Glittenberg C; Považay B; Drexler W; Graf A;Binder S. Human Retinal Pigment Epithelium (Rpe) Transplantation: Outcome after Autologous Rpe-Choroid Sheet and Rpe

Cell-Suspension in a Randomised Clinical Study. Br J Ophthalmol 95, 370–375 (2011). [PubMed: 20610478]

7. van Zeeburg EJT; Maaijwee KJM; Missotten TOAR; Heimann H;van Meurs JC A Free Retinal Pigment Epithelium–Choroid Graft in Patients with Exudative Age-Related Macular Degeneration: Results up to 7 Years. American Journal of Ophthalmology 153, 120–127.e122, (2012). [PubMed: 21907969]
8. West EL; Ribeiro J;Ali RR Development of Stem Cell Therapies for Retinal Degeneration. Cold Spring Harb. Perspect. Biol 12, a035683 (2020).
9. Ricles LM; Hsieh P-L; Dana N; Rybalko V; Kraynak C; Farrar RP;Suggs LJ Therapeutic Assessment of Mesenchymal Stem Cells Delivered within a Pegylated Fibrin Gel Following an Ischemic Injury. Biomaterials 102, 9–19 (2016). [PubMed: 27318932]
10. Santiesteban DY; Kubelick K; Dhada KS; Dumani D; Suggs L;Emelianov S. Monitoring/Imaging and Regenerative Agents for Enhancing Tissue Engineering Characterization and Therapies. Annu. Biomed. Eng 44, 750–772 (2016).
11. Rogers WJ; Meyer CH;Kramer CM Technology Insight: In Vivo Cell Tracking by Use of Mri. Nat. Clin. Pract. Cardiovasc. Med 3, 554–562 (2006). [PubMed: 16990841]
12. Scarfe L; Brillant N; Kumar JD; Ali N; Alrumayh A; Amali M; Barbellion S; Jones V; Niemeijer M;Potdevin S. Preclinical Imaging Methods for Assessing the Safety and Efficacy of Regenerative Medicine Therapies. *NPJ* Regen. Med 2, 1–13 (2017).
13. Sheikh AY;Wu JC Molecular Imaging of Cardiac Stem Cell Transplantation. Curr. Cardiol. Rep 8, 147–154 (2006). [PubMed: 16524542]
14. Wolfs E; Verfaillie CM; Van Laere K;Deroose CM Radiolabeling Strategies for Radionuclide Imaging of Stem Cells. Stem Cell Rev. Rep 11, 254–274 (2015). [PubMed: 25534590]
15. Dhada KS; Hernandez DS;Suggs LJ In Vivo Photoacoustic Tracking of Mesenchymal Stem Cell Viability. ACS nano 13, 7791–7799 (2019). [PubMed: 31250647]
16. Donnelly EM; Kubelick KP; Dumani DS;Emelianov SY Photoacoustic Image-Guided Delivery of Plasmonic-Nanoparticle-Labeled Mesenchymal Stem Cells to the Spinal Cord. Nano Lett. 18, 6625–6632 (2018). [PubMed: 30160124]
17. Jokerst JV; Thangaraj M; Kempen PJ; Sinclair R;Gambhir SS Photoacoustic Imaging of Mesenchymal Stem Cells in Living Mice Via Silica-Coated Gold Nanorods. ACS nano 6, 5920–5930 (2012). [PubMed: 22681633]
18. Zhang W; Li Y; Nguyen VP; Huang Z; Liu Z; Wang X;Paulus YM High-Resolution, in Vivo Multimodal Photoacoustic Microscopy, Optical Coherence Tomography, and Fluorescence Microscopy Imaging of Rabbit Retinal Neovascularization. Light Sci. Appl 7, 103 (2018). [PubMed: 30534372]
19. Nguyen VP; Li Y; Zhang W; Wang X;Paulus YM High-Resolution Multimodal Photoacoustic Microscopy and Optical Coherence Tomography Image-Guided Laser Induced Branch Retinal Vein Occlusion in Living Rabbits. Sci. Rep 9, 10560 (2019). [PubMed: 31332266]
20. Zhang L; Song W; Shao D; Zhang S; Desai M; Ness S; Roy S;Yi J. Volumetric Fluorescence Retinal Imaging in Vivo over a 30-Degree Field of View by Oblique Scanning Laser Ophthalmoscopy (Oslo). Biomed. Opt. Express 9, 25–40 (2018). [PubMed: 29359085]
21. Nguyen VP; Li Y; Qian W; Liu B; Tian C; Zhang W; Huang Z; Ponduri A; Tarnowski M;Wang X. Contrast Agent Enhanced Multimodal Photoacoustic Microscopy and Optical Coherence Tomography for Imaging of Rabbit Choroidal and Retinal Vessels in Vivo. Sci. Rep 9, 5945 (2019). [PubMed: 30976009]
22. Kubelick KP; Snider EJ; Ethier CR;Emelianov S. Development of a Stem Cell Tracking Platform for Ophthalmic Applications Using Ultrasound and Photoacoustic Imaging. Theranostics 9, 3812 (2019). [PubMed: 31281515]
23. Tian C; Zhang W; Mordovanakis A; Wang X;Paulus YM Noninvasive Chorioretinal Imaging in Living Rabbits Using Integrated Photoacoustic Microscopy and Optical Coherence Tomography. Opt. Express 25, 15947–15955 (2017). [PubMed: 28789105]
24. Krohne TU; Westenskow PD; Kurihara T; Friedlander DF; Lehmann M; Dorsey AL; Li W; Zhu S; Schultz A;Wang J. Generation of Retinal Pigment Epithelial Cells from Small Molecules and Oct4

Reprogrammed Human Induced Pluripotent Stem Cells. Stem Cells Transl. Med 1, 96–109 (2012). [PubMed: 22532929]

25. Li Y; Zhang W; Nguyen VP; Rosen R; Wang X; Xia X;Paulus YM Real-Time Oct Guidance and Multimodal Imaging Monitoring of Subretinal Injection Induced Choroidal Neovascularization in Rabbit Eyes. Exp. Eye Res 186, 107714 (2019).
26. Cho EC; Zhang Q;Xia Y. The Effect of Sedimentation and Diffusion on Cellular Uptake of Gold Nanoparticles. Nat. Nanotechnol 6, 385 (2011). [PubMed: 21516092]
27. Nel A; Xia T; Mädler L;Li N. Toxic Potential of Materials at the Nanolevel. science 311, 622–627 (2006). [PubMed: 16456071]
28. Barnett JM; Penn JS;Jayagopal A. in Nanobiotechnology Protocols 45–56 (Springer, 2013).
29. da Silva HR; Mamani JB; Nucci MP; Nucci LP; Kondo AT; Fantacini DMC; de Souza LEB; Picanço-Castro V; Covas DT; Kutner JM; de Oliveira FA; Hamerschlak N;Gamarra LF Triple-Modal Imaging of Stem-Cells Labeled with Multimodal Nanoparticles, Applied in a Stroke Model. World J Stem Cells 11, 100–123 (2019). [PubMed: 30842808]
30. Ansi Z136.1. https://www.lia.org/store/product/ansi-z1361-2014-safe-use-lasers-electronic-version (2007).
31. Kuo T-R; Hovhannisyan VA; Chao Y-C; Chao S-L; Chiang S-J; Lin S-J; Dong C-Y;Chen C-C Multiple Release Kinetics of Targeted Drug from Gold Nanorod Embedded Polyelectrolyte Conjugates Induced by near-Infrared Laser Irradiation. J. Am. Chem. Soc 132, 14163–14171 (2010). [PubMed: 20857981]
32. Organisciak DT;Vaughan DK Retinal Light Damage: Mechanisms and Protection. Prog Retin Ey Res 29, 113–134 (2010).
33. Robinson D. The Mechanics of Human Saccadic Eye Movement. J. Physiol 174, 245–264 (1964). [PubMed: 14244121]
34. Song W; Wei Q; Liu T; Kuai D; Zhang HF; Burke JM;Jiao S. Integrating Photoacoustic Ophthalmoscopy with Scanning Laser Ophthalmoscopy, Optical Coherence Tomography, and Fluorescein Angiography for a Multimodal Retinal Imaging Platform. J. Biomed. Opt 17, 061206 (2012).
35. Nguyen VP; Qian W; Li Y; Liu B; Aaberg M; Henry J; Zhang W; Wang X;Paulus YM Chain-Like Gold Nanoparticle Clusters for Multimodal Photoacoustic Microscopy and Optical Coherence Tomography Enhanced Molecular Imaging. Nat. Commun 12, 34 (2021). [PubMed: 33397947]
36. Qian W; Murakami M; Ichikawa Y;Che Y. Highly Efficient and Controllable Pegylation of Gold Nanoparticles Prepared by Femtosecond Laser Ablation in Water. The J. Phys. Chem C 115, 23293–23298 (2011).
37. Nguyen VP; Li Y; Zhang W; Wang X;Paulus YM Multi-Wavelength, En-Face Photoacoustic Microscopy and Optical Coherence Tomography Imaging for Early and Selective Detection of Laser Induced Retinal Vein Occlusion. Biomed. Opt. Express 9, 5915–5938 (2018). [PubMed: 31065403]
38. Tian C; Zhang W; Nguyen VP; Wang X;Paulus YM Novel Photoacoustic Microscopy and Optical Coherence Tomography Dual-Modality Chorioretinal Imaging in Living Rabbit Eyes. J. Vis. Exp. JOVE 132, 57135 (2018).

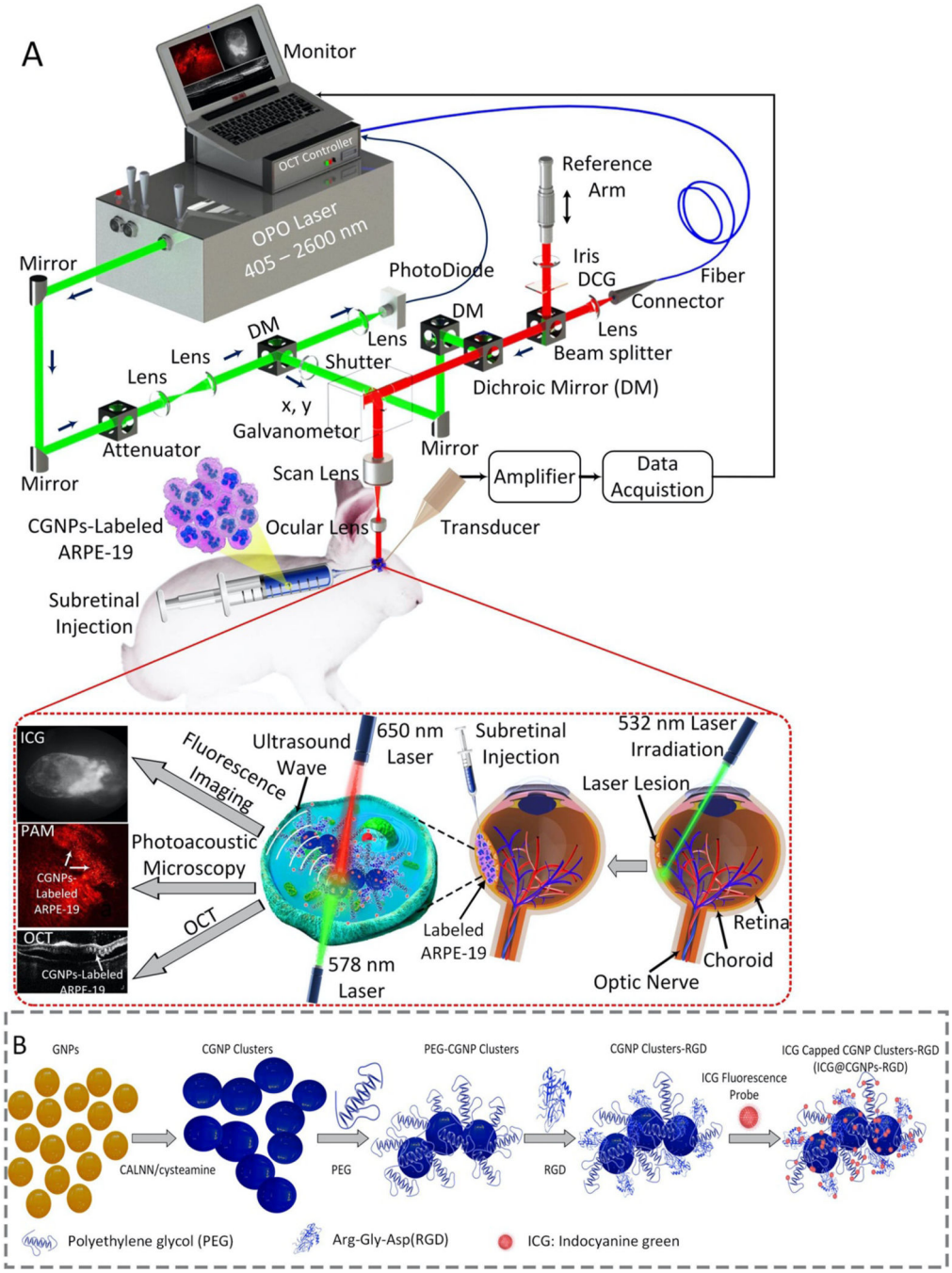

Figure 1. Custom-built PAM, OCT, and fluorescence multimodality imaging system, stem cell transplantation procedure and synthesis procedure of functionalized chain-like gold nanoparticles clusters:

(**A**) Schematic diagram of the imaging system and *in vivo* experiment protocol. Green laser photocoagulation was performed to induce RPE and retinal injury. Then, multi-modality PAM and OCT imaging were used to monitor the labeled ARPE-19 cells injected into the subretinal space for 90 days post-injection. Two different excitation wavelengths of 578 nm and 650 nm were applied to acquire PAM images. (**B**) Schematic diagram of ICG@CGNP clusters-RGD synthesis.

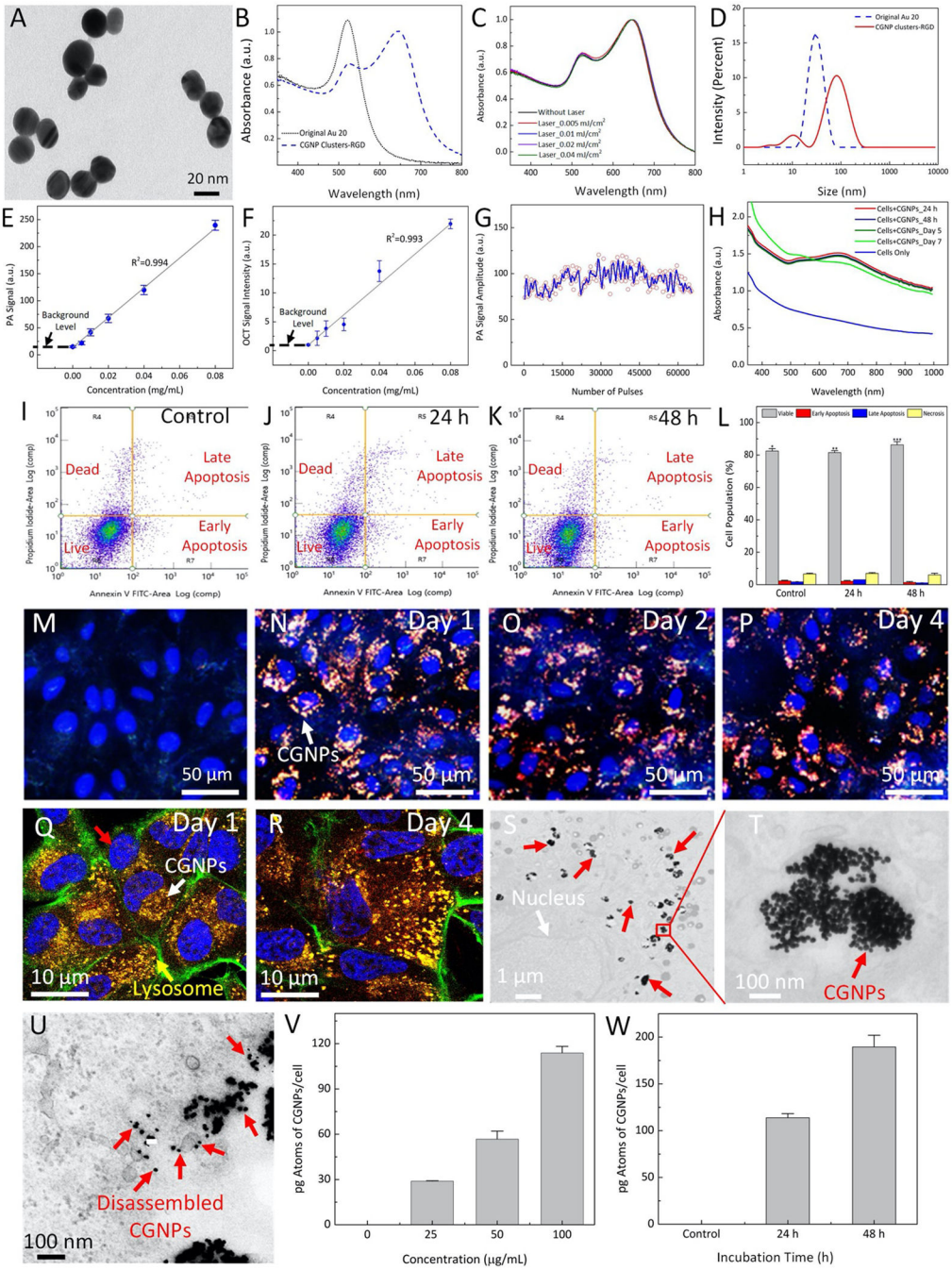

Figure 2. Characterization of chain-like gold nanoparticles clusters (CGNP clusters-RGD and ICG@ CGNP clusters-RGD), optical properties, and biocompatible analysis:

(**A**) TEM image of CGNP clusters-RGD (×2000, 20 kV; bar = 200 nm). (**B**) UV-Vis spectrum of GNPs and CGNP clusters-RGD in DI water. (**C**) UV-Vis spectrum of CGNP clusters-RGD before and after being illuminated for 5 min by nanosecond pulsed laser at various pulse energies (0.005, 0.01, 0.02, and 0.04 mJ/cm^2), demonstrating excellent photostability. (**D**) Hydrodynamic size distribution of GNPs and CGNP clusters-RGD in DI water characterized by using dynamic light scattering (DLS). (**E**) *In vitro* PA signal intensity

as a function of CGNP clusters-RGD mass concentration. (**F**) *In vitro* OCT signal intensity as a function of CGNP clusters-RGD concentrations. (**G**) *In vitro* photoacoustic signals from CGNP clusters-RGD when illuminated continuously by a total of 65,000 pulses at fluence of 0.01 mJ/cm^2 at a wavelength of 650 nm. Blue line shows the average PA signal. (**H**) UV-Vis spectra of fixed ARPE-19 cells after being incubated with CGNP clusters-RGD at a concentration of 100 μg/mL (red line) and original ARPE-19 cells (blue line). Only slight change in spectrum was noticed after day 7 (green line). (**I–K**) Flow cytometry analysis of three different groups: control (**I**), treated with CGNP clusters-RGD for 24 hrs (**J**) and treated with CGNP clusters-RGD for 48 hrs (**K**). (**L**) Quantification of cell population. (**M–P**) Light scattering dark-field images of ARPE-19 cells before and after being incubated with ICG@CGNP clusters-RGD at a concentration of 100 μg/mL for 1, 2, and 4 days. (**Q–R**) fixed ARPE-19 cells after being incubated with CGNP clusters-RGD for 24 hrs and 96 hrs, respectively. Green fluorescent color shows the f-actin stained by phalloidin. The cell's lysosomes were stained by lysotracker (yellow arrow). Red fluorescent signal indicates the distribution of internalized CGNP clusters inside the cells (white arrow). Blue color shows the cell's nuclei were stained by DAPI (red arrow). (**S–T**) Transmission electron microscopy (TEM) images of ARPE-19 cells. The cells were treated with CGNP clusters-RGD at concentration of 100 μg/mL and incubated for 24 hrs. White arrow shows the position of nucleus whereas the red arrows indicate the internalized CGNPs inside the cells. The scale bars are (**S**) 1 μm and (**T**) 50 nm. (U). TEM image of treated cells for 96 hrs. Red arrows show the location of disassembled GNPs. (**V**) Quantification the amount of internalized CGNP clusters inside ARPE-19 cells as a function of CGNP clusters concentrations using ICP-MS. (**W**) Quantification of the amount of CGNP clusters inside single cell. All error bars represent the standard deviation (N = 3).

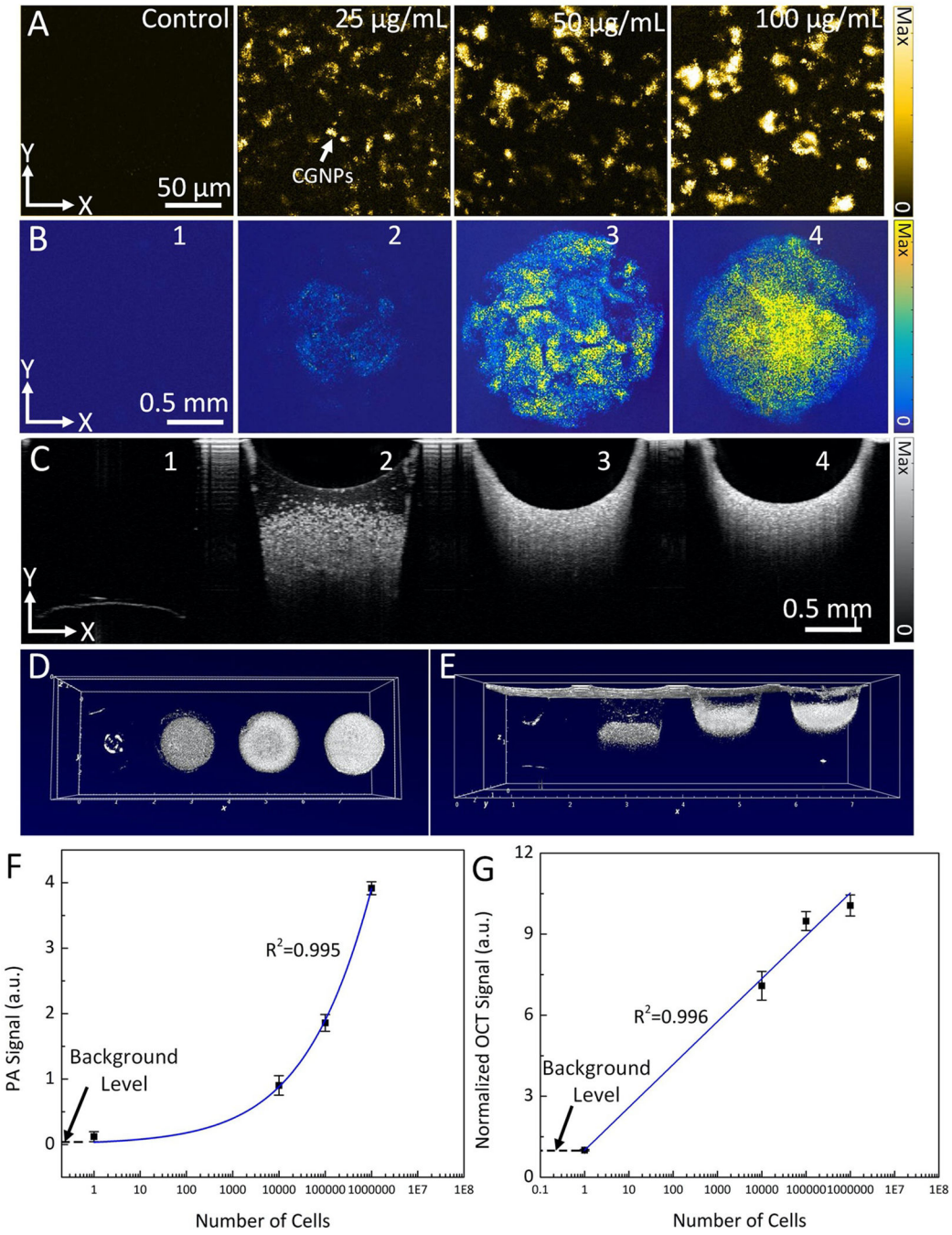

Figure 3. ***In vitro*** **validation of CGNPs labeled cells for PAM and OCT imaging:**
(**A**) *In vitro* PAM images of fixed ARPE-19 cells labeled with CGNP clusters-RGD at different concentrations (i.e., 0 (control), 25, 50, and 100 μg/mL) acquired at the excitation wavelength of 650 nm. (**B**) In *vitro* PAM images of fixed cells labeled with CGNP clusters-RGD in agarose mimicking-phantom at different cells concentrations (10^1, 10^4, 10^5, and 10^6 cell/mL). The PAM images acquired at the excitation wavelength of 650 nm. (**C–E**) OCT images of fixed cells in 2D (**C**) and 3D perspective (**D–E**). (**F–G**) Quantitative PAM and OCT signals as a function of cell concentration, respectively. PAM signal amplitude

increases linearly with cell concentration. Error bars indicate the standard deviation of three independent measurements (N=3).

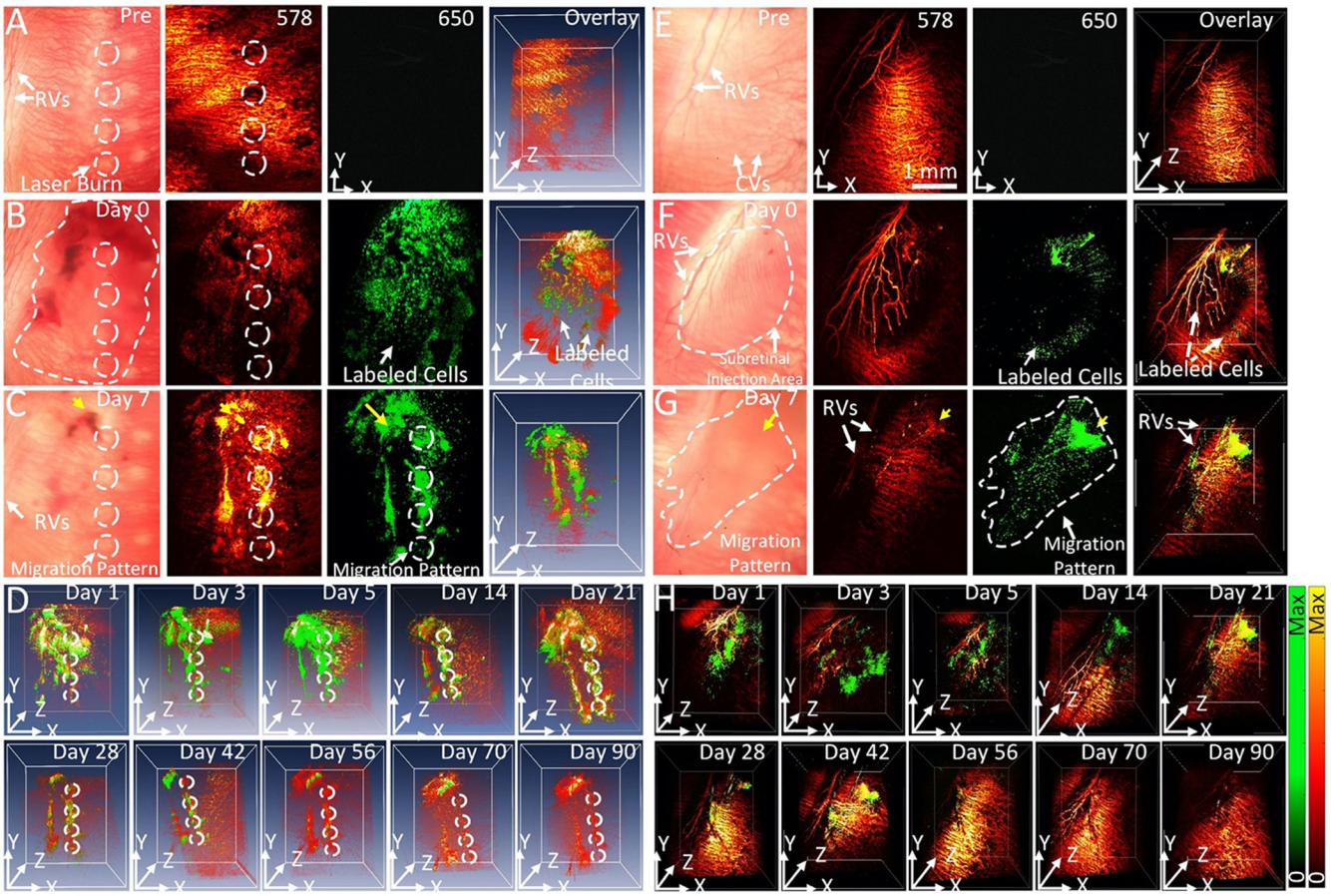

Figure 4. ***In vivo*** **PAM images of labeled ARPE-19 cells post-transplantation into rabbit retina: (A)–(D)** *In vivo* PAM images of CGNP clusters-labeled ARPE-19 cells post-transplantation into rabbit eyes with laser-induced RPE injury. **(A)** Baseline fundus photograph and PAM images acquired at 578 nm and 650 nm before the transplantation of the ARPE-19 cells. White arrows indicate the locations of retinal vessels (RVs) and photocoagulation lesions. **(B–D)** 2D and 3D volumetric PAM images of the ARPE-19 cells acquired at different time points post-transplantation, illustrating cell viability and migration toward photocoagulation lesions. The dotted line in **(B)** indicates the distribution of ARPE-19 cells post-transplantation, while the dotted circles in **(A–C)** show the lesion areas. The pseudo green color in PAM images acquired at 650 nm shows the distribution of the transplanted ARPE-19 cells. See Supplementary Visualization 3 for 3D volumetric presentation. **(E–H)** *In vivo* PAM images of CGNP clusters-labeled ARPE-19 cells post-transplantation into rabbit eyes without laser-induced RPE injury. **(E)** Fundus photograph and PAM images acquired at 578 nm and 650 nm before the transplantation of ARPE-19 cells. **(F–H)** 2D and 3D volumetric PAM images acquired at different time points post-transplantation, illustrating cell viability and migration in a random fashion. The dotted line in **(F)** indicates the distribution of cells immediately post-injection, while the dotted line in **(G)** illustrates cell migration over time. See Supplementary Visualization S4, S5, and S6 for 3D volumetric presentation.

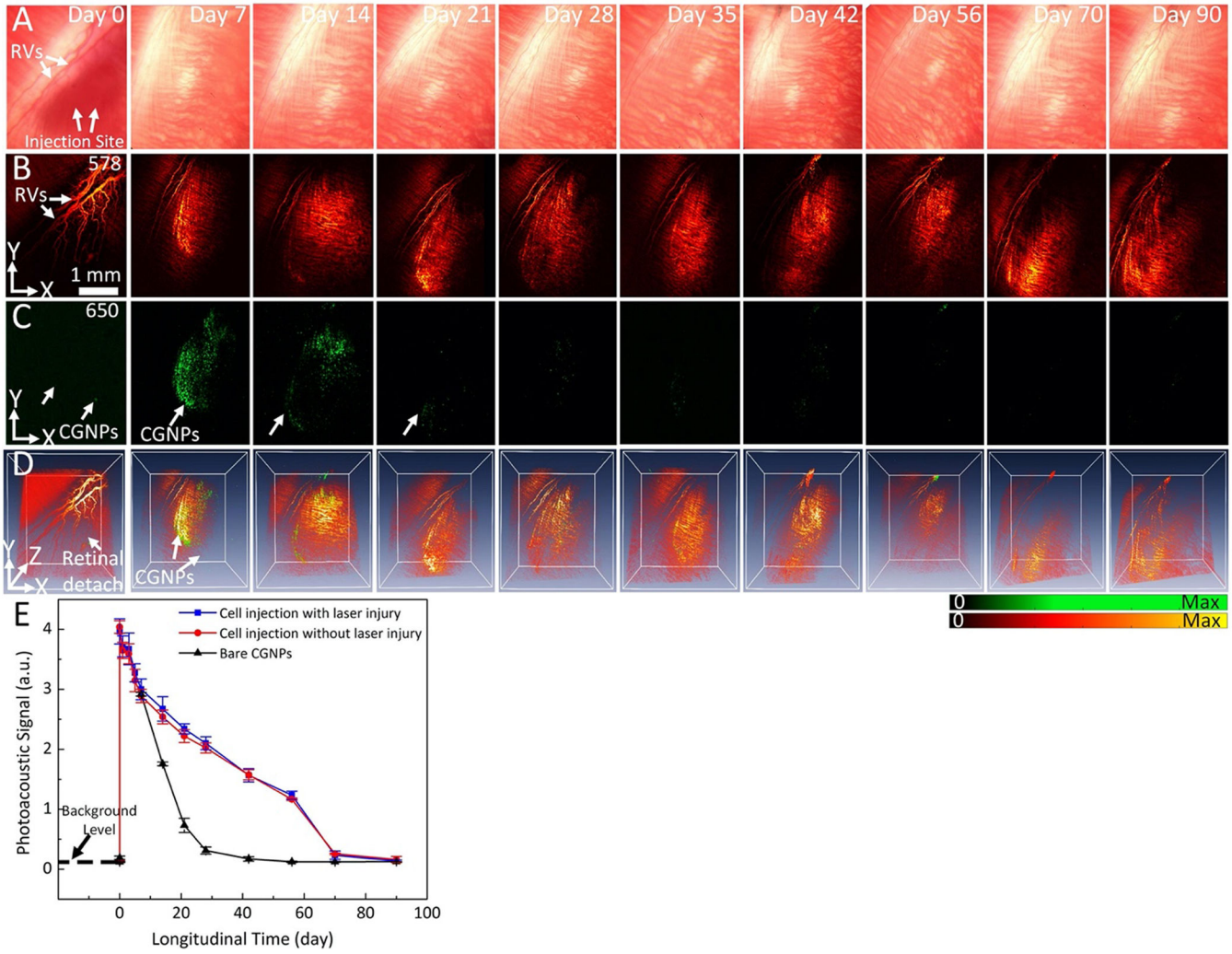

Figure 5. ***In vivo*** **kinetic evaluation of CGNP clusters in living rabbits using PAM imaging:** (**A**) Color fundus photograph of the rabbit retina imaged immediately post-injection of CGNPs at a concentration of 20 μg/mL and followed for up to 90 days. White arrows show the location of the CGNP clusters distributed in the subretinal space and retinal vessels (RVs). (**B**) and (**C**) Corresponding PAM images acquired at 578 nm and 650 nm, respectively. The images acquired at 578 nm show clearly retinal vasculature whereas only CGNP clusters are shown in PAM image acquired at 650 nm (pseudo green color). (**D**) Overlay 3D images. See Supplementary Visualization 5 for 3D presentation. (**E**) Graph comparing the quantified PAM signals induced by subretinally injected CGNP clusters-labeled cells and subretinally injected free CGNP clusters *in vivo*, showing the difference in PAM signal decreasing over time. The error bars represent standard error (N=3), $p<0.001$.

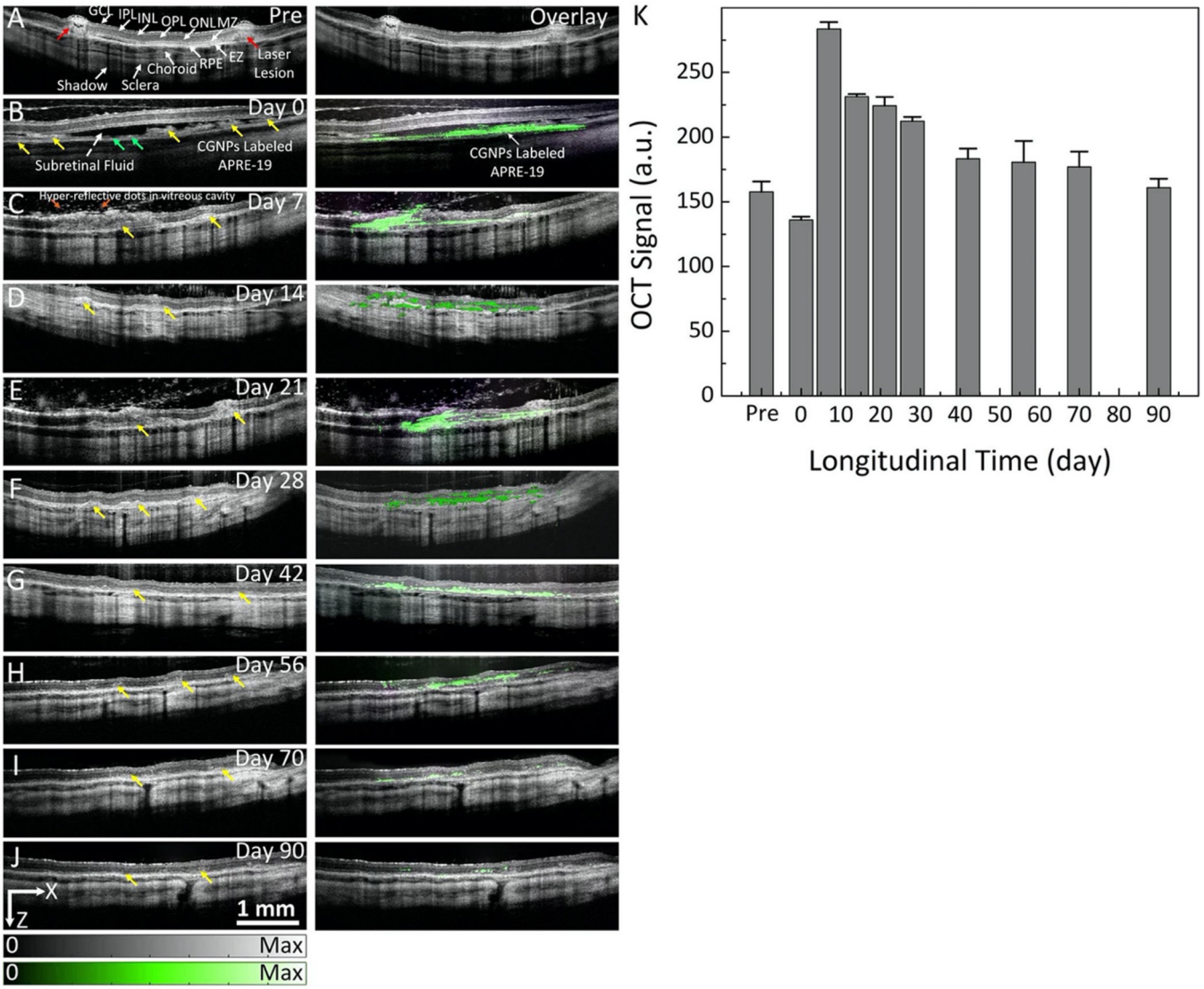

Figure 6. ***In vivo*** **OCT visualization of CGNP clusters-RGD-labeled ARPE-19 cells in rabbit eyes:** (**A**) B-scan OCT image and OCT image overlaid with PAM image acquired at 650 nm before transplantation of ARPE-19 cells. Retinal layers and laser injury sites are clearly observed with high spatial resolution and high contrast. There is no PA signal observed prior to ARPE-19 cell transplantation. (**B–J**) Selection of OCT images and OCT and PAM overlay images acquired on day 0 (**B**), day 7 (**C**), day 14 (**D**), day 21(**E**), day 28 (**F**), day 42 (**G**), day 56 (**H**), day 70 (**I**), and day 90 (**J**) after ARPE-19 cell transplantation, respectively. Green arrows show the distribution of ARPE-19 cells in the subretinal space immediately post-transplantation with high contrast as shown in (**B**) (left-side) and co-registered with PAM signal (right-side). Noted that the migration of the ARPE-19 cells into the injured sites can be observed in PAM images clearly, as shown by the pseudo green color. (**K**) Quantitative OCT signal intensity as a function of time. The error bars represent the standard error (N=3), $p<0.05$.

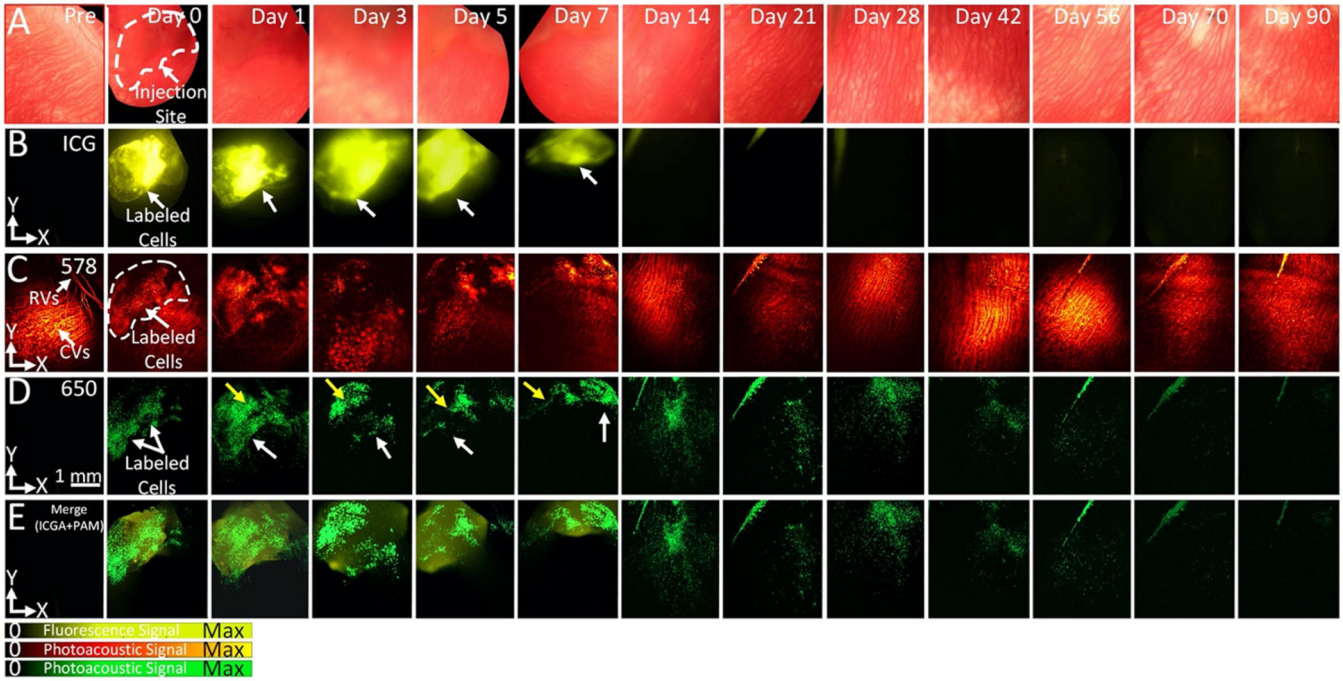

Figure 7. Triple modality imaging for identification of ICG@CGNP clusters-RGD-labeled ARPE-19 cells in rabbit eyes *in vivo*:

(**A**) Color fundus images prior- and post-injection of ARPE-19 cells obtained by color fundus photography at different time points ranging from day 0 to day 90. (**B–E**) Visualization of transplanted ARPE-19 cells at various time points from immediately post-injection (Day 0) to over 90 days. As shown in (**B**), cells labelled with ICG@CGNP clusters-RGD were clearly identified with excellent fluorescence contrast (white dotted line) post-injection. Similarly, the PAM images acquired at 578 nm and 650 nm show high image contrast, and cells were easy discriminated from the native choroidal vessels at 650 nm (green color). No signal was observed in ICG fluorescence image and PAM image at 650 nm before injection. ICG fluorescence imaging and PAM were correlated well on the overlay images in (**E**). Note that the fluorescence signal rapidly reduced and was nearly invisible at day 14 post-injection. In contrast, PAM images show significant contrast for up to 56 days and then PAM signal reduced thereafter.

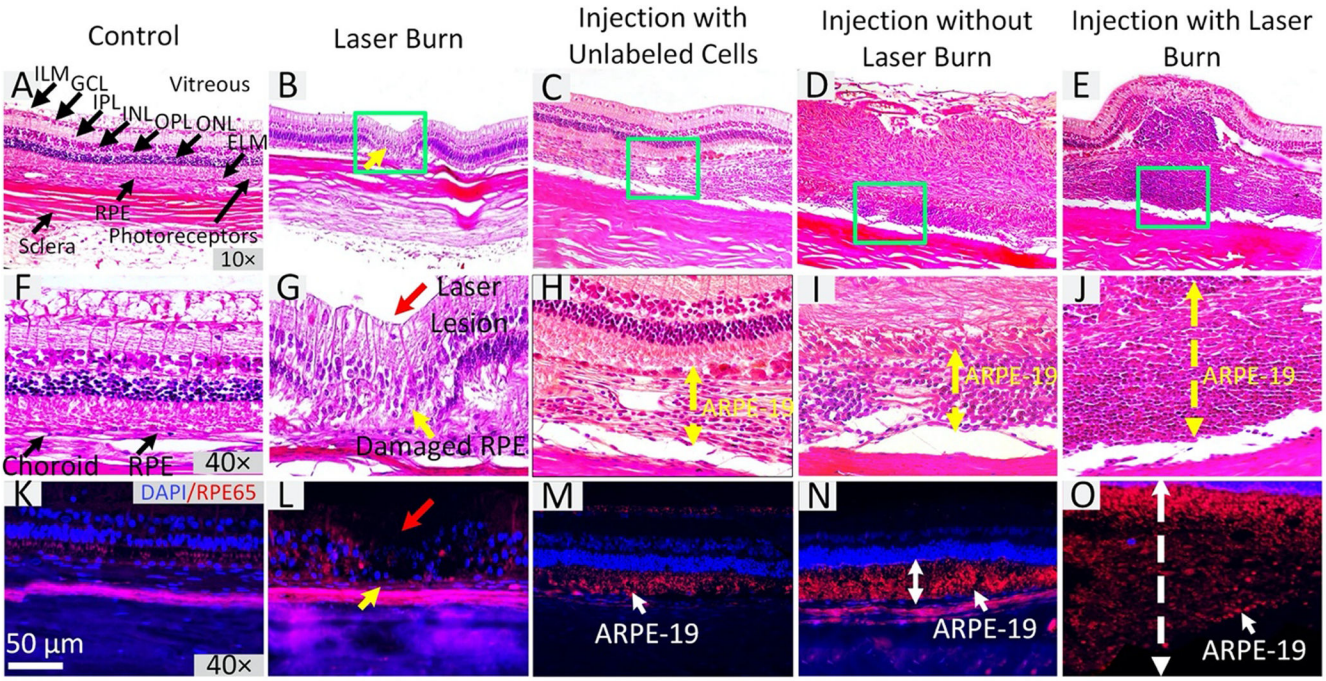

Figure 8. Immunohistochemistry and Histological Validation:

Rabbit tissue sections were stained with RPE65 to visualize the distribution of human RPE cells. Hematoxylin and eosin (H&E) staining images of control group (**A**) 10× and (**F**) 40×. These images show no evidence of retinal destruction with normal cell morphology. Each retinal layer is clearly visible. (**B–E**) and (**G–J**) H&E staining for laser-induced injury without cell transplantation, subretinal transplantation of non-labeled ARPE-19 cells, subretinal transplantation of CGNP clusters- labeled ARPE-19 cells into rabbits without having local laser injury, and subretinal transplantation of CGNP clusters-labeled ARPE-19 cells into rabbits with local laser injury, respectively. Large RPE layers are present on treated tissues 90 days post-transplantation (**C–E** and **H–J**). The RPE layer and retina showed significant changes (yellow arrows). Red arrow shows the position of laser injury. (**K–O**) Immunostaining for RPE65 provides evidence of human RPE (red fluorescence color) in subretinal space and growth at the laser injuries. Blue fluorescence color indicates the cell nuclei stained by DAPI.

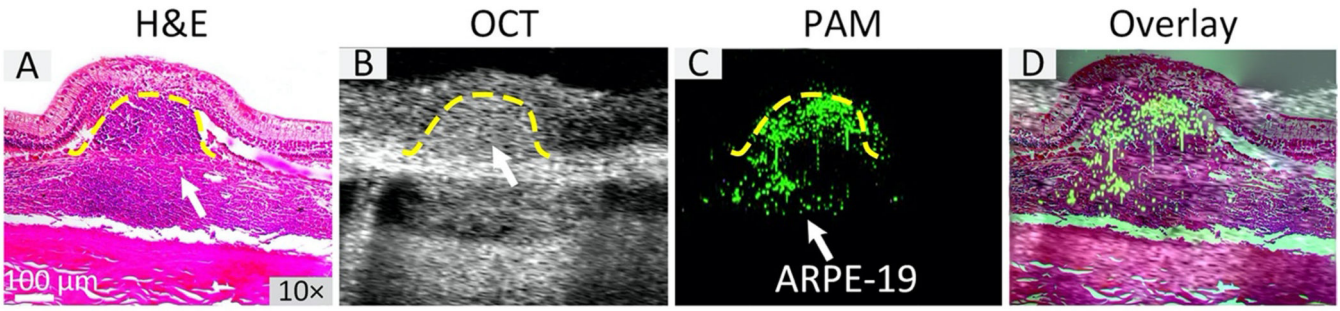

Figure 9. Correlation of H&E, PAM, and OCT imaging:

B-scan OCT (**B**) and PAM (**C**) were co-registered with H&E image (**A**) on the same image planes to visualize the migration of the transplanted cells at laser injury sites as well as to confirm the capability of multi-modality PAM and OCT for precisely mapping the locations of cells after transplantation. The overlay image (**D**) verified the presence of ARPE-19 cells detected by PAM located at same areas obtained by H&E and OCT.

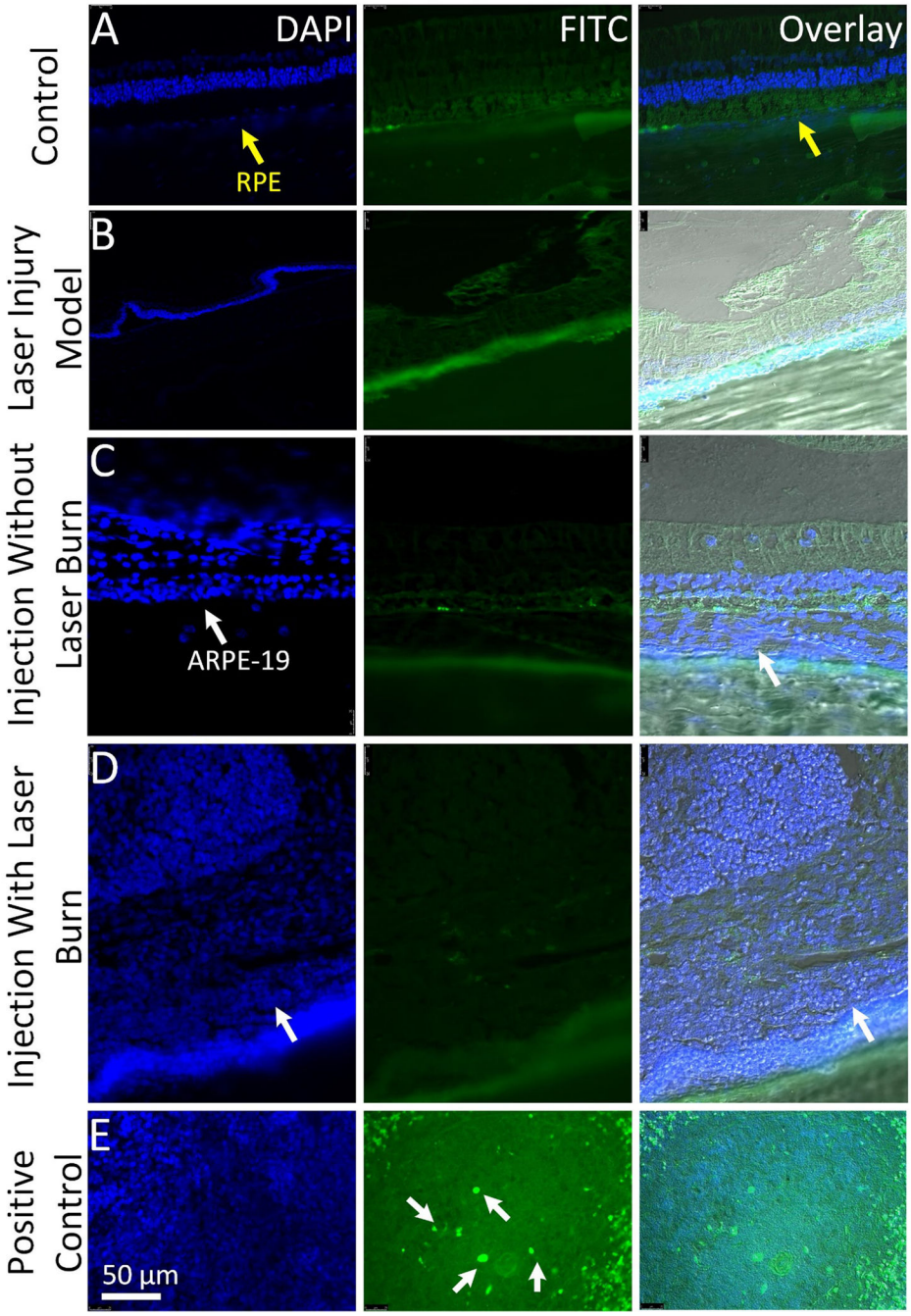

Figure 10. ***In vivo*** **biosafety analysis:**

(A-D) TUNEL assay analysis obtained at 3-month post ARPE-19 cells transplantation. Six-micrometer sections from different retinal tissues (control, laser-induced injury without ARPE-19 cells injection, cell injection without laser-induced injury, and cells injection with laser-induced injury) stained for FITC to examine the apoptotic cells and DAPI (blue) to visualize cell nuclei. No apoptosis-positive cells were observed in the transplanted retinal

tissues. (E) Positive control shows FITC-labeled apoptotic cells (white arrows). Scale bar: 50 μm.